Geomorphology 485 (2025) 109835

Contents lists available at ScienceDirect

Geomorphology

journal homepage: www.journals.elsevier.com/geomorphology

Dynamic characteristics and erosion mechanisms of debris flows triggered by ice avalanches

Xiangning Li, Jiangang Chen *, Xiaoqing Chen *, Xi'an Wang, Jinshui Wang, Hechun Ruan, Min Huang

Key Laboratory of Mountain Hazards and Earth Surface Process, Institute of Mountain Hazards and Environment, Chinese Academy of Sciences (CAS), Chengdu 610041, China
University of Chinese Academy Sciences, Beijing 100049, China

ARTICLE INFO

Keywords:
Debris flows triggered by ice avalanches
Flow regime
Basal stress
Flow dynamics
Entrainment mechanism

ABSTRACT

Debris flows triggered by ice avalanches (abbreviated as *DFIs*) are a common catastrophic hazard in alpine regions, and their flow regimes may vary with ice content. Previous studies have focused mainly on the deposition characteristics, mobility, and hazard assessments of *DFIs*; however, no systematic investigations have focused on the basal stress characteristics and erosion mechanisms. In this study, a series of flume experiments were conducted to investigate the effects of the ice content on the flow regime and stress of a *DFI* during erosion. The results revealed that the flow regime of the *DFI* changed from friction-dominated to viscous/collisional-dominated flows with increasing ice content. Ice clearly contributed to the increase in flow velocity during erosion, whereas the effects on flow depth, stress and pore pressure were not significant. The erosion rate of *DFIs* was found to be independent of the water content of the bed and related to flow infiltration. Erosion affected only the uppermost soil particles, which immediately became saturated once *DFIs* flowed over them. Therefore, the critical Shields number can be used to describe the resistance of an initial soil bed to erosion, as the surficial soil particles are saturated by infiltrated flow. The shear stress exerted by the *DFI* can be directly measured, and then the erosion rate can be obtained. A comparison between the measured and calculated erosion rates of the methods in this study, those of a single-phase erosion model, and those of a two-phase erosion model proved that the results of our study were appropriate for describing the erosive forces of the *DFI*.

1. Introduction

The alpine mountains are becoming an important site for the construction of major projects (Shen et al., 2022). With the completion of some major projects, the glacier-related disasters will seriously threaten the engineering infrastructure and the safety of people's lives and properties in the region (Shen et al., 2022). Glacial debris flow is the typical glacier disaster, which can be divided into several types. Among them, *DFIs* are one of the more representative types. These are characterized by large volumes, long movement distances and strong destructiveness and occur mostly in the areas in which hanging glaciers are developing (Li et al., 2022a, 2022b; Peng et al., 2022). Therefore, we need to focus on the behaviour of *DFIs*.

The occurrence of *DFIs* have been more frequent over the past few decades, causing severe disasters. On February 7, 2021, a large rock-ice avalanche triggered a debris flow in the Chamoli district, Uttarakhand, India (Van Wyk de Vries et al., 2022). A 26.9 Mm^3 wedge composed of approximately 80 % bedrock and 20 % glacier ice detached from the north face of Ronti Mountain. This wedge dropped approximately 1800 m to the Ronti Gad valley floor, where it continued downvalley towards the Rishiganga and Dhauliganga rivers and became a debris flow. The resulting debris flow left 204 missing or dead and destroyed two hydropower stations. On October 16, 2018, the Sedongpu event was one of the largest *DFI* events that occurred in the Namcha Barwa–Gyala Peri massif in recent decades in China. This event lasted for 480 s. The event originated as a huge landslide on the east side of Gyala Peri, with an initial total of about 6 Mm^3 of rock and ice material, with a low ice content. The landslide deposits travelled downstream and triggered this

* Corresponding authors at: Key Laboratory of Mountain Hazards and Earth Surface Process, Institute of Mountain Hazards and Environment, Chinese Academy of Sciences (CAS), Chengdu 610041, China.
E-mail addresses: lixiangning@imde.ac.cn (X. Li), chenjg@imde.ac.cn (J. Chen), xqchen@imde.ac.cn (X. Chen), wangxian@imde.ac.cn (X. Wang), wangjs@imde.ac.cn (J. Wang), ruanhechun@imde.ac.cn (H. Ruan), minhuang@imde.ac.cn (M. Huang).

https://doi.org/10.1016/j.geomorph.2025.109835
Received 29 July 2024; Received in revised form 29 March 2025; Accepted 10 May 2025
Available online 20 May 2025

DFI. The *DFI* slowed and then crept to the bottom of Sedongpu gully, finally blocking the Yarlung Zangbo River (Wang et al., 2019; Zhang et al., 2022; Zhao et al., 2022). In addition, severe glacial debris flows occurred in September 2007, July 2010, September 2010, and July 2018 in Tianmo gully, Tibet Plateau, China. Among them, the debris flow that occurred in July 2018 was a typical *DFI*. It initiated from an ice avalanche on the southeast side of the glacier, released approximately 2.77×10^6 m^3 of rock and ice materials, and transformed into a debris flow downstream of the gully (Ge et al., 2014; Guo et al., 2023). Finally, debris flows with large ice blocks have blocked the Parlung Zangpo River (Gao et al., 2019). It is clear from these events that ice exist in *DFIs* and that the ice content is typically 20–60 % (Evans et al., 2009; Shugar et al., 2021; Van Wyk de Vries et al., 2021; Zhou et al., 2024).

Due to the effect of global warming on the temperature amplification in high-altitude mountain areas (De et al., 2013), glacial permafrost has been in a state of rapid ablation and retreat in recent decades (Haeberli et al., 2017; Monnier and Kinnard, 2015).

It further leads to an increase in the frequency and volume of *DIFs* outbreaks (Li et al., 2022a, 2022b). To mitigate *DIF* hazards, its movement characteristics and erosion mechanism must be studied to provide a scientific basis for minimizing its adverse impact on key infrastructures.

Remote sensing methods have been used to identify and evaluate *DFI* hazards in previous studies (Guo et al., 2023; Li et al., 2022a, 2022b). Combined satellite remote sensing, meteorological observations, numerical modelling, and post-event field investigation, evolution processes and potential triggers of *DFIs* were comprehensively analysed. The dynamic process of *DFIs* has been shown via numerical simulations, and the effects of ice on the mobility of *DFIs* have been discussed (Wang et al., 2023; Zhou et al., 2024). The results showed that the initial ice/water content is critical to the mobility of the *DFI* in the initial and later transport stage, while the phase transition only plays a minor role (Wang et al., 2023). This will occur when ice content of *DFI* is less. However, if the initial ice content was relatively high, the melting of the ice during its movement due to the change of temperature during the movement deserves further study. Pudasaini (2024) have proposed the new model offering the first-ever complete dynamical solution for simulating rock-ice avalanche with changing temperature. This demonstrated that ice melting and entrainment significantly enhanced the mobility of *DFIs* (Pudasaini and Fischer, 2020a; Pudasaini, 2024). Significant phase separation as the flow transforms driven by density, size and friction differences between ice and rock have an important influence on the mobility of *DFIs* (Pudasaini and Fischer, 2020a; Pudasaini and Fischer, 2020b; Zhou et al., 2024). Existing studies are mainly based on numerical simulations to analyse the erosion mechanism of *DFIs* (Pudasaini, 2024; Wang et al., 2023). However, fewer studies have used modelling experiments to investigate the erosion characteristics of *DFIs*.

Flow and bed conditions jointly control erosion (de Haas et al., 2022; Pudasaini and Fischer, 2020a; Pudasaini, 2022, 2024). Flow conditions that describe the cumulative forces exerted at the bed over the full event (flow volume, flow composition and cumulative shear stress) have the correlations with erosion. When the gravel content of the flow increases, the flow velocity decreases and shear and collision stresses increase, leading to increased erosion. Different erosion mechanisms dominate under debris flows with different compositions (Roelofs et al., 2022). This is because variation in the material composition of the fluid changes the internal stresses in the fluid, which in turn affects erosion (Pudasaini and Fischer, 2020a; Pudasaini, 2022, 2024). Bed conditions describe the effect of the bed soil composition (de Haas et al., 2022; Pudasaini and Fischer, 2020a; Pudasaini, 2022, 2024; Roelofs et al., 2023), particle size distribution (Li et al., 2022a, 2022b) and wetness (Iverson et al., 2010; Ng et al., 2022; Song and Choi, 2021) on erosion. When debris flows move through the bed surface, it will induce changes in the pore pressure of the bed soils. This is related to the water content of the bed soils. Previous studies have shown that there is not a linear relationship between pore pressure of the bed soil and its water content. This is related to the different permeability of the bed soil resulting from changes in bed soil water content (Roelofs et al., 2023; Zheng et al., 2024).

Previous studies have illustrated the erosion mechanisms based on the theoretical analysis. Basically, two types of erosion models are used: empirical and mechanical ones. Empirical laws have been developed based on empirical methods and are most used in practice, but without physical basis. The relationship between erosion rate and gully characterization parameters, flow depth and velocity are established (Christen et al., 2010; McDougall and Hungr, 2005). Empirical laws have some limitations, because these are not physical. Process-based mechanical models are derived with the mass and momentum exchanges between a debris flow and the underlying erodible bed (Pudasaini, 2012; Pudasaini and Fischer, 2020a). This model show that the erosion rate is related to the shear stress difference between entraining and resisting stresses, and the flow velocity. Erosion model can be divided into two categories: single-phase (Iverson, 2012) and two-phase or multi-phase model (Pudasaini, 2022; Pudasaini, 2024). The two-phase or multi-phase model erosion model is required for better describing the physical mechanics of the phenomena.

The above methods have been widely applied to no ice debris flows (Li et al., 2024; Zheng et al., 2021). Previous studies on *DFIs* have investigated only their dynamic process via numerical simulations and have not determined the relationships between the erosion rate and mechanical parameters on the basis of theoretical and experimental approaches (Peng et al., 2022; Wang et al., 2023). Physical modelling experiments and theoretical analyses have been used to explore the basal stress characteristics of rock–ice avalanches and have revealed the relationships between the ice content and basal stress (Dong and Su, 2024; Dong et al., 2024; Pudasaini and Krautblatter, 2014; Pudasaini, 2024; Schneider et al., 2011; Wang et al., 2022). These relationships provide important insight into *DFI* studies, showing that the dynamic characteristics of *DFIs* can be investigated through modelling experiments and theoretical analysis, and the effects of the ice content on their mobility can be investigated.

Therefore, a flume test was conducted to explore the stress characteristics and erosion mechanisms of *DFIs*. This study aimed to answer the following questions: (1) How do basal stresses vary with the ice content of the *DFI*? (2) How does ice affect the flow regime of a *DFI*? (3) What is the erosion mechanics of *DFI*? The findings presented in this paper are expected to advance knowledge on the flow behaviors and dynamics of *DFIs*.

2. Experimental setup and materials

2.1. Experimental setup and instrumentation

A typical flume was used to investigate the dynamics and erosion mechanisms of *DFIs* (Fig. 1). The flume was 4 m in length, 0.3 m in width, and 0.4 m in height (Fig. 1a). The length of the flume is generally selected as 2–8 m in the previous studies (Ng et al., 2022; Song and Choi, 2021; Zheng et al., 2021), which is applicable to be uses in this study. The width of the flume should be more than five times larger than the largest particle of debris flow material (Sun et al., 2022). It is chosen as 0.3 m with reference to previous studies. The flume was fixed at an angle α of 18° to the horizontal plane according to the *DFI* in Tianmo gully and the critical conditions when erosion occurred (Takahashi, 2007; Breien et al., 2008; Guo et al., 2023). The mean slope of Tianmo gully is 16°. And erosion occurred on gradients of 15–21° (Breien et al., 2008). Therefore, the channel slope of the flume is defined as 18°.

The upstream end of the flume was isolated as a storage container with an uplift gate for the release of debris material. The channel bed consisted of a nonerodible section to accelerate the flow, and a section with an erodible soil bed. The nonerodible section had a length of 2 m. The erodible section had a length and depth of 1.5 m and 0.12 m, respectively. At the downstream end of the flume, the flow was collected in a tank to ensure that it did not influence the kinematic and dynamic

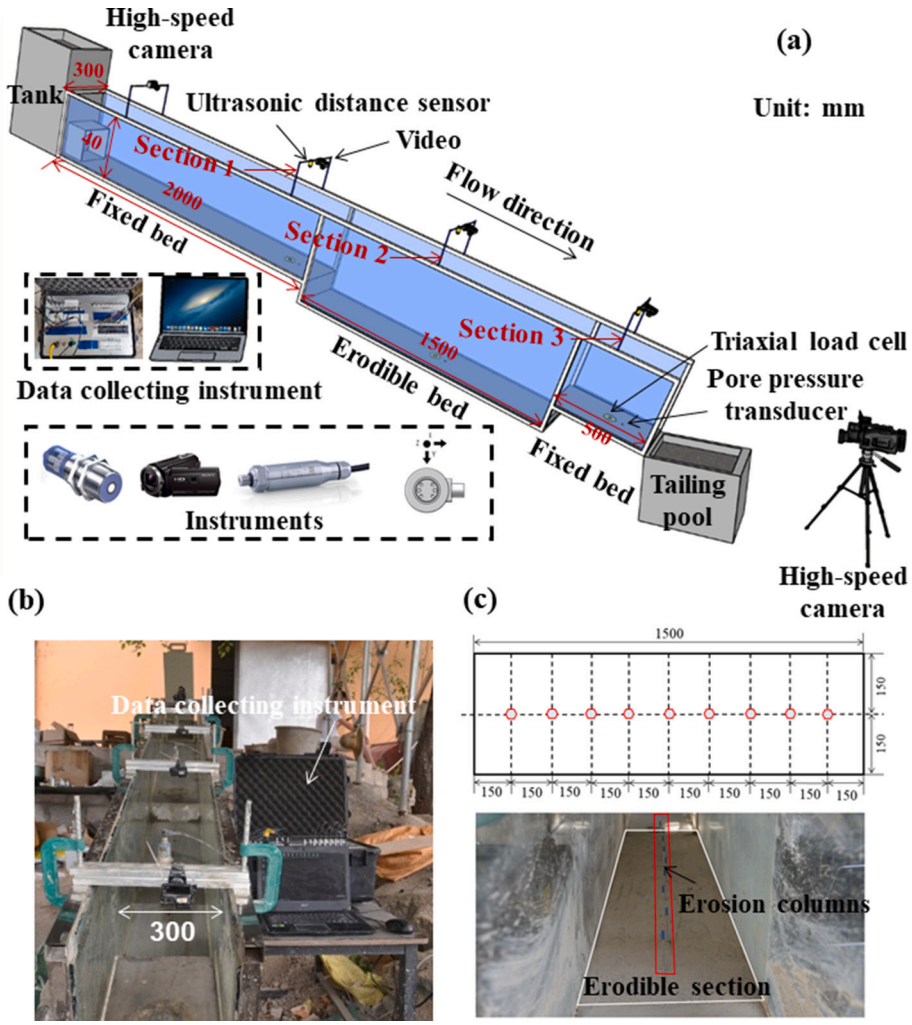

Fig. 1. Schematic diagram of the experimental apparatus. (a) Flume setup and instruments; (b) photograph of the flume setup; (c) plan layout of the erosion columns. All dimensions are in millimetres.

properties of the ensuing flow. The 0.05m^3 of *DFI* material, released from the storage container, applied shear stress to the unsaturated soil bed that was eroded as a result of the *DFI*. The *DFI* was composed of ice and a two-phase mixture of soil and water. The solid volume concentration of the two-phase mixture of soil and water kept constant, which was determined as 0.3. The ice contents of *DFI* were controlled by changing the volume ratio of ice and the two-phase mixture of soil and water.

The parameters measured in the test included the normal stress, shear stress, pore pressure, flow depth, velocity, and erosion depth. The normal and shear stresses of the flume bed were measured via a series of triaxial load cells (LH-SZ-02). Three observation sections were prepared in the flume bed. Section 1 was located downstream of the nonerodible section. The distance between the circular hole for installing the triaxial load cell and the upstream part of the erodible section was 0.2 m. Section 2 was 0.8 m away from the upstream part of the erodible section, where the centre of the sensor circle was located. Section 3 was located upstream of the other nonerodible section, 231.5 mm away from the bottom of the flume. Pore pressure transducers (JUL-P31, 10 kPa, ±0.1 % F. S.) were installed downstream of the triaxial load cell, and the centre of its location was 66.5 mm from the centre of the triaxial load cell. Ultrasonic sensors (U-GAGE T30UX) and a high-speed camera were set above the triaxial load cell to measure the flow depth and velocity. All sensor data were collected with a data collection instrument, with a sampling rate of 500 Hz to ensure data accuracy. (Fig. 1b).

The erosion columns buried in the soil beds were used to measure the erosion depth. Each erosion column was constructed with a stack of 40 hexagonal nuts. Each nut was 3 mm in height and 7 mm in width (Fig. 1c). The nuts were threaded through rods that were removable from the base of the erodible bed. The erosion columns were spaced 15 cm apart along the centreline of the erodible section. They were initially prepared to the same height as the initial elevation of the soil bed. The soil bed was then prepared. Afterwards, the rods were removed without disturbing the nut columns or soil bed. During each test, the nuts near the surface of the erodible bed were carried away along with the soil beds. The erosion depth was deduced from the difference in the height of the columns before and after the test.

2.2. Materials and test program

Tianmo gully is located in Bomi County, Tibet Autonomous Region, China, and is a typical area in which *DFIs* develop. Many studies have focused on this area to study disasters related to glaciers (Ge et al., 2014; Guo et al., 2023; Zhou et al., 2019). The samples used for the tests were collected from the depositional area of Tianmo gully. This is the deposition formed by multiple *DFI*, and is a reliable composition of *DFI*. A maximum particle size of 20 mm of the test materials was selected for the experiment. The grain size compositions of the test materials are shown in Fig. 2. The coefficient of uniformity was 63, and the coefficient of curvature was 1.29. The median particle size was 0.81 mm. The

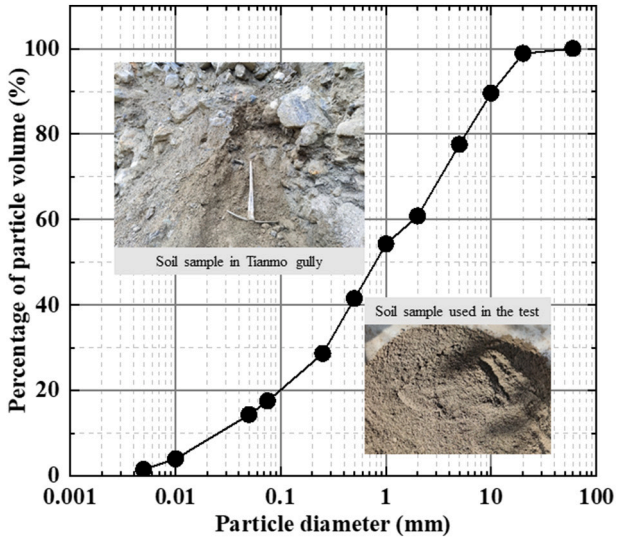

Fig. 2. Gradation curve of particles in soil for the experiment.

erodible bed has the same grain size composition as the debris flow mixture. Table 1 shows the physical properties of the solid and fluid phases within the *DFI* and bed sediments. Here, ρ, ρ_s^m, ρ_f^m, μ_s^m, α_s^m, α_f^m are the bulk density, solid grain density, fluid phase density, effective Coulomb friction coefficient, solid volume fraction and fluid volume fraction of the released debris flow respectively. ρ^b, ρ_s^b, ρ_f^b, μ_s^b, α_s^b, α_f^b are the six corresponding counterparts of the underlying bed sediment. These parameters and variables are defined based on the work of Pudasaini and Fischer (2020a) and Pudasaini (2024). The fluid phase density is much complex. The fluid is composed of water and very fine particles. And the fluid phase is governed by its true density, viscosity, and isotropic stress distribution (Pudasaini and Mergili, 2019). It can be calculated based on the method adopted by (Iverson, 1997). The value of μ_s^m is a weighted average of the Coulomb friction coefficients of the soil-water two-phase mixture and the ice. The Coulomb friction coefficients of the soil-water two-phase mixture is estimated as 0.466 according to the previous literatures (Pudasaini, 2022), which is determined as 0.12 for ice followed by the results of Dong and Su (2024). The value of μ_s^b is taken as the ratio of shear stress to normal stress measured in the erodible bed.

The ice contents in *DFIs* are lower than those in ice–rock avalanches, in which the ice contents generally do not exceed 20 % (Peng et al., 2022; Wang et al., 2023). The influence of the ice–water phase transition on the dynamics of *DFIs* is minor. Therefore, the ice contents of the *DFI* were set to 0 %, 5 %, 10 %, 15 % and 20 %. This depends on the volume ratio of ice and the two-phase mixture. Following the methods of Wang et al. (2022) and Yang et al. (2019), the size of ice cubes was 20 mm × 20 mm × 20 mm, which was the same as the maximum size of debris flow materials.

All sensors are installed in their specified locations. The *DFI* materials were subsequently prepared. The soil beds with a certain water content were placed in the erodible section in a loose state. The six bed soil water content were set at 0, 5 %, 8 %, 10 %, 12 % and 14 %, respectively. In the experiment, In the experiment, a *DFI* of the same ice content eroded the bed soils of each of the six water contents, and then erosion characteristics were analysed. The erosion columns were buried inside the sediment according to the plan layout shown in Fig. 1c. After the soil bed was prepared, the rods were removed vertically (Berger et al., 2011). The soil and ice materials were mixed in the flume storage container to ensure that the *DFI* materials were uniformly mixed. During this process, an electric mixer was firstly used to mix the two-phase mixture of soil and water, and then poured it into the tank. Next, the prepared ice cubes were also poured into the tank. After 10 s of rapid stirring using manual stirring method, it was found that ice and the two-phase mixture of soil and water had been mixed homogeneously. Therefore, the stirring time of the *DFI* mixtures was determined as 10s in each experiment. This can ensure adequate mixing of the *DFI* materials on the one hand, and on the other hand reduce the amount of ice melt. Due to the short stirring time, the ice cubes were essentially undamaged and no melting occurred.

Finally, the *DFI* was initiated by lifting the gate to the container and releasing the mixtures. During the tests, the plastic balls with a diameter of 20 mm and the density much less than that of water, ice and *DFI* were thrown into the flume. It has no effect on the motion characteristics of the *DFI* and it can move with the *DFI* due to its low density and mass. The movement of the *DFI* was recorded by a high-speed camera. The movement time of the plastic balls at a certain distance of movement was obtained through analysing the video frame by frame and thus the frontal velocity of the *DFI*.

2.3. Data reduction

To evaluate the flow dynamics of experimental and natural debris flows, six dimensionless parameters were used: the Froude number (*Fr*), Bagnold number (N_B), Savage number (N_S), friction number (N_{fric}), mass number (N_M), and Reynolds number (N_R) (Iverson, 1997, 2015). The dimensionless parameters characterize the flow regime of a debris flow. They are able to characterize the macro-behavioural forces in fluids, the solid-phase forces between particles at the micro-scale of debris flows, and the solid-liquid coupling between particles and fluids. The important aspects related to complex heat exchange processes within the fluid, heat conduction at the sliding base and enhancement of the temperature due to the entrainment of the basal material need to be considered during *DFI* propagation (Pudasaini, 2024). The experiment of this study was conducted at a shorter spatial and temporal dimension. And ice content of *DFI* is less. The effects of ice melting and heat exchange process on erosion is minor (Wang et al., 2023). Therefore, variation of temperature was not considered. Six dimensionless parameters can be used to characterize the similarity between the experiments and real events. And the same approach has been adopted in previous studies (Dong and Su, 2024; Schneider et al., 2011; Zheng et al., 2021).

The data in Section 1 were used for calculations. N_{Fr} represents the ratio of the flow inertia and gravity, can be expressed as follows:

$$N_{Fr} = \frac{v}{\sqrt{gh\cos\theta}} \tag{1}$$

Table 1
Physical properties of the *DFI* and bed sediments for each experimental condition.

No.	Debris flow							Bed sediment					
	Ice content	ρ (kg/m^3)	ρ_s^m (kg/m^3)	ρ_f^m (kg/m^3)	μ_s^m	α_s^m	α_f^m	water content	ρ^b (kg/m^3)	ρ_s^b (kg/m^3)	ρ_f^b (kg/m^3)	α_s^b	α_f^b
1	0.00	1528.0	2760.0	1332.0	0.47	0.14	0.86	0.00	1648.15	2760	1000	1.00	0.000
2	0.05	1497.6	2250.1	1332.0	0.37	0.18	0.82	0.05	1315.74	2760	1000	0.94	0.003
3	0.10	1467.2	1936.9	1332.0	0.31	0.22	0.78	0.08	1361.11	2760	1000	0.90	0.005
4	0.15	1436.8	1725.1	1332.0	0.27	0.27	0.73	0.10	1428.70	2760	1000	0.87	0.007
5	0.20	1406.4	1572.2	1332.0	0.24	0.31	0.69	0.12	1555.56	2760	1000	0.83	0.009
6	/	/	/			/	/	0.14	1702.78	2760	1000	0.79	0.011

where v is the velocity of the *DFI* (m/s); h is the flow depth of the *DFI* (m); g is the gravitational acceleration (m/s^2); and θ is the inclination of the flume channel (°). Following the work of Choi et al. (2015), the *Fr* in the field ranges from 0.5 to 7.6. In this study, the *Fr* ranged from 1.4 to 6.7, similar to the values in previous studies (Song et al., 2021a, 2021b, 2023).

N_B characterizes the ratio of stress generated via instantaneous grain collision and viscous shear stress:

$$N_B = \frac{\upsilon_s \rho_s \delta^2 \dot{\gamma}}{\upsilon_f \eta} \tag{2}$$

where υ_s is the volume fraction of the solid. ρ_s is the average solid particle density. δ (m) is the characteristic grain size equal to D_{50}. In this study, D_{50} is the weighted average characteristic grain size of the soil and ice cubes. $\dot{\gamma}$ is the shear rate calculated by v/h. υ_f (equal to (1-υ_s)) is the volume fraction of fluid. η (Pa·s) is the fluid viscosity. The solid particle density ρ_s represents the combination of the soil density ρ_r and the ice density ρ_i and can be expressed as follows:

$$\rho_s = \rho_r \upsilon_s + \rho_i \upsilon_i \tag{3}$$

The interstitial fluid viscosity can be estimated as follows (de Haas et al., 2015; Roelofs et al., 2023):

$$\frac{\eta}{\eta_w} = 1 + 2.5\upsilon_{fines} + 10.05{\upsilon_{fines}}^2 + 0.00273^{16.6\upsilon_{fines}} \tag{4}$$

where η_w is the dynamic viscosity of pure water (0.001002 Pa·s). υ_{fines} is the volume fraction of the interstitial fluid occupied by fines.

The density of the interstitial fluid ρ_f is defined as the combined density of pure water and fines (Iverson, 1997):

$$\rho_f = \rho_r \upsilon_{fines} + \rho_w (1 - \upsilon_{fines}) \tag{5}$$

The ratio of collisional to frictional forces is defined by the Savage number (N_S):

$$N_s = \frac{\rho_s \delta^2 \dot{\gamma}^2}{(\rho_s - \rho_f) g h} \tag{6}$$

The ratio of frictional to viscous forces is defined by the friction number (N_{fric}):

$$N_{fric} = \frac{N_B}{N_S} = \frac{\upsilon_s}{1 - \upsilon_s} \frac{(\rho_s - \rho_f) g h}{\dot{\gamma} \eta} \tag{7}$$

N_M characterizes the ratio of solid inertia to fluid inertia and can be expressed as follows:

$$N_M = \frac{\upsilon_s}{1 - \upsilon_s} \frac{\rho_s}{\rho_f} \tag{8}$$

N_R defines the ratio between the solid inertial stress and the viscous shear stress of the fluid:

$$N_R = \frac{\rho_f \dot{\gamma} D_{50}^2}{\eta} \tag{9}$$

To characterize the spatial scour pattern, the scour asymmetry ratio (A_{me}) was introduced (de Haas and Woerkom, 2016). Scour asymmetry is defined as the ratio between the maximum scour depth in the upper (x = 0–0.5 L) and lower halves (x = 0.5–L) of the erodible section:

$$A_{me} = \frac{H_{e,x=0-0.5L}}{H_{e,x=0.5-L}} \tag{10}$$

Where H_e is the erosion depth (m). Asymmetry values above 1 indicate more erosion in the upper half of the bed, whereas values below 1 imply the opposite.

2.4. Data acquisition and processing

A *DFI* is a complex multiphase fluid with a complicated dynamic process. Significant fluctuations can be found in the stress and flow depth. The random pulsation characteristics of the data can be caused by the mechanical vibration and interference of the microcurrent of the data acquisition system during the experiments. Therefore, the implementation of noise reduction processing on the monitored raw signal is necessary. We removed the high-frequency fluctuations by averaging the data over ten points (0.01 s). When the ice content of the *DFI* and the water content of the soil bed were zero, the comparison between the normal stress at Section 1 before and after the filter is illustrated in Fig. 3.

3. Results and interpretation

3.1. Effects of the ice content on the flow regime of incoming flows

Different ice contents of the fluid were used in the experiment. The effects of the ice content on all the dimensionless parameters were considered. The values of the dimensionless parameters are listed in Table 2. Fig. 4 shows the relationships between the dimensionless parameters and ice contents. All the dimensionless parameters, except N_{Fr}, increased with increasing ice content. The N_{Fr} values ranged from 2.76 to 4.49. The *DFIs* were all supercritical flows ($N_{Fr} > 1$), dominated by the inertial force. N_{Fr} decreased with increasing ice content, which was influenced by the flow depth.

The N_B values were >200 when the ice contents ranged from 5 % to 20 %, meaning that collisional forces dominated viscous forces. When no ice existed in the *DFI*, viscous forces dominated. These results are consistent with those of a previous study (Zheng et al., 2021). When ice was present in the fluid, the N_B increased significantly. The flow regime transformed into collision-dominated flow. Dong et al. (2024) used a drum test to investigate the dynamics of rock–ice avalanches and reported consistent results. The D_{50} increased significantly with increasing ice content. This resulted in increased N_B.

N_s was <0.1 when the ice content was zero. The flow regime was dominated by frictional stress. N_s was >0.1 when ice was present. N_s reached 2.83 at 20 % ice content. The flow regime transformed into dominated by grain collisions. This also resulted from the increase in D_{50}.

N_{fric} values ranged from 553.37 to 833.56 and were more than those in 100 for different ice contents. The flow regime was dominated by frictional stress. This finding on the basis of the variations of N_B, N_S and N_{fric}, showed that three main stress states were present in the *DFI*, namely, particle collision stress > friction stress > viscous stress.

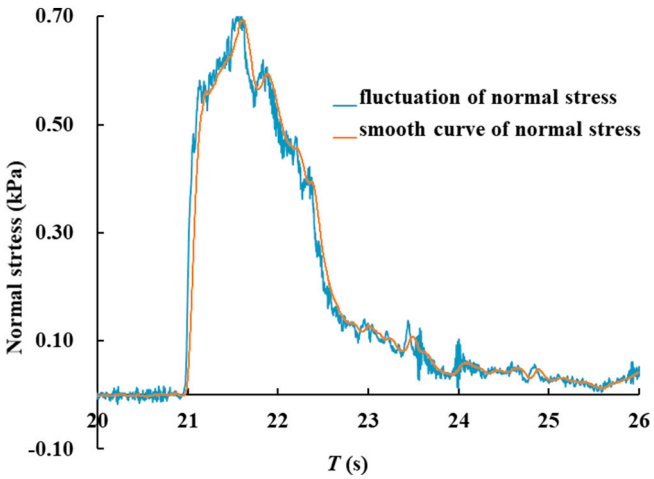

Fig. 3. Smooth curve normal and fluctuating normal stress.

Table 2
The A_{me} values varied with the ice content for the soil beds with different water contents.

Ice content	Water content of the bed soil					
	0.00	0.05	0.08	0.10	0.12	0.14
0.00	1.62	1.50	2.00	1.50	1.80	1.43
0.05	1.69	1.40	1.45	1.31	2.86	1.90
0.10	1.20	0.82	0.82	1.00	1.64	1.60
0.15	1.58	1.36	1.78	1.60	1.27	1.67
0.20	1.85	1.63	1.11	1.25	1.80	1.75

N_M increased with increasing ice content. These values were less than unity for different ice contents. The flow regime transformed into fluid-dominated flow. The N_R values were >1 and increased with increasing ice content. The results revealed a mixed mechanism of viscous shear stress and grain collisions in the flow regime. However, the flow regime was still dominated by grain collisions.

3.2. Effects of the ice content on the flow kinematics of DFIs

3.2.1. Flow depth variation of DFI during erosion

Fig. 5 shows the variation of the flow depth of *DFI* with different ice contents as the water content of soil beds varies from 0 to 14 %. The composition and density of the *DFI* changed when ice existed. However, the presence of ice had a relatively small effect on the flow depth. The flow depth basically stabilized at 0.037–0.040 m for the different ice contents. When the *DFI* flowed over Section 2, the soil bed eroded. The flow depth changed with soil beds with different water contents. The flow depth increased with the movement of the *DFI* when the water content of the soil bed was <0.08. The lower the ice content was, the greater the increase in flow depth. The flow depth increased by 5.4 % ~ 51.4 % with different water contents and zero ice content. When the water content of the bed soils is low, the soils strengthen are weak and easy to be eroded. Therefore, the flow depth will increase at section 2. When ice content is low, the flow depth was greater compared to high ice content, due to the higher volume of the soil-water two-phase mixture. This was resulting from the more significantly effects of the water content of the *DFI* on the flow depth. These results were consistent with the research of Wang et al. (2023). The *DFI* had a large erosive capacity. Momentum and potential energy were gained in erosion, which induced the mobility of *DFI* increase. Therefore, the erosive capacity of the *DFI* was greater (Pudasaini and Fischer, 2020a; Pudasaini and Krautblatter, 2021). When the water content of the soil bed was >0.08, the flow depth decreased with increasing ice content, except at a 5 % ice content. The flow depth reached a minimum of 0.031 m when the water content of the soil bed was 0.14. Section 3 was the location of post-erosion observations. The flow depth did not significantly change compared with that in Section 2. This finding illustrated that the effects of erosion on the flow depth were minor downstream of the erodible section. However, the flow depth increased significantly compared with that in Section 1. The maximum increase was approximately 0.29 times.

3.2.2. Flow velocity variation of DFI during erosion

Fig. 6 shows the relationships among the velocity, ice content, and water content of the soil beds. For ice contents of 0 % and 10 %, the velocity reached maxima of 2.61 and 2.72 m/s, respectively. The velocity ranged from 1.66 to 1.83 m/s for *DFIs* with different ice contents. When the *DFI* flowed over Section 2, the velocity increased for different ice contents, i.e., increased by 5.5 % ~ 89.0 %. The velocity increased

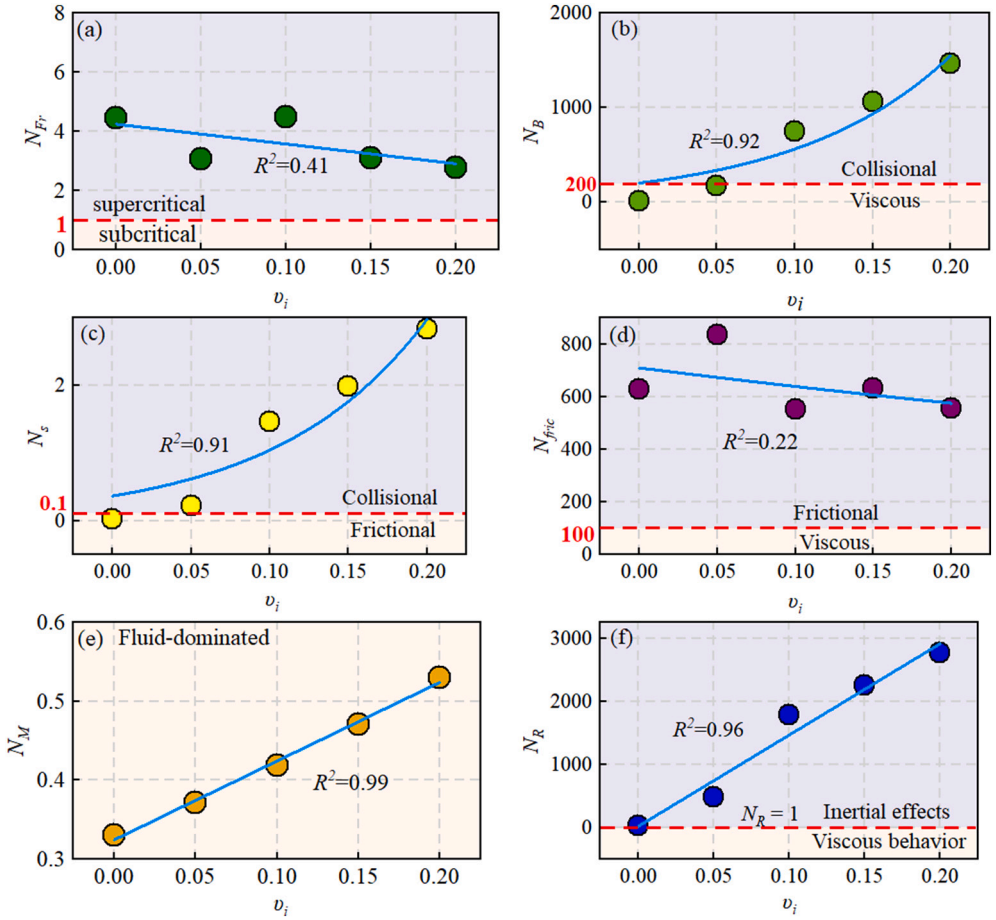

Fig. 4. Relationships among N_{Fr}, N_B, N_S, N_{fric}, N_M, N_R and v_i.

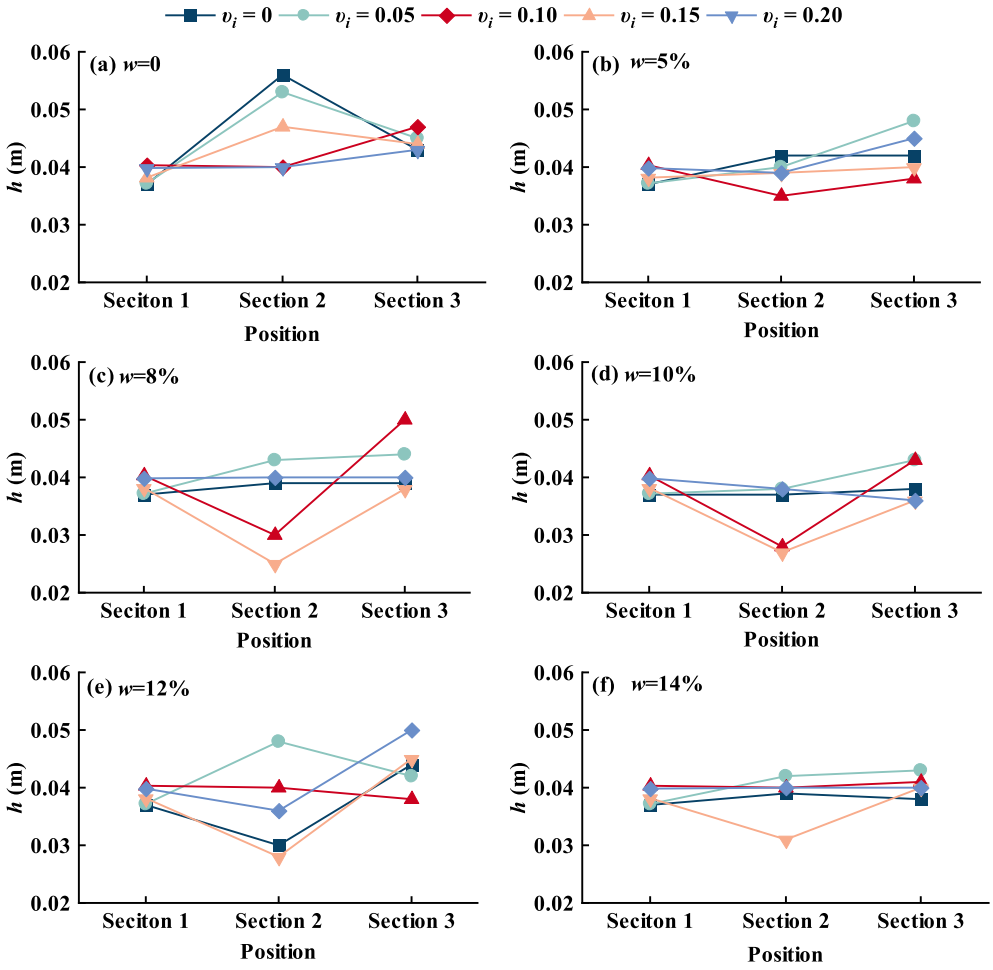

Fig. 5. Relationships among the flow depth, ice content, and water content of the soil beds in the different observation sections. (a)-(f) The water content of bed soil was 0, 5 %, 8 %, 10 %, 12 % and 14 %, respectively.

the most, from 60.1 % to 89.0 %, for a 20 % ice content. After the *DFI* flowed over the erodible section, the velocity did not vary significantly with the ice content compared with that in Section 2. However, the velocity in Section 3 was higher than that in Section 1 and increased by 12.3 % ~ 99.6 %. This finding showed that erosion significantly enhanced the mobility of the *DFI*.

3.2.3. *Basal stress variation of DFI during erosion*

The normal stress and shear stress are mechanical parameters that indicate the erosive capacity of a debris flow. For soil beds with different water contents, the effects of the ice content on the normal stress and the shear stress were similar. The shear stress first increased but then decreased along the channel. The shear stress reached a maximum in the erodible section. The normal stress exhibited the opposite result. The normal stress reached a minimum in the erodible section.

Fig. 7 shows the variations in the shear stress for the soil beds with an 8 % water content. In Fig. 7a~7e, the ice contents increased from 0 % to 20 %. For different ice contents, the shear stresses of the erodible section reached maxima of 0.124, 0.208, 0.121, 0.18 and 0.299 kPa, respectively. The shear stress in Section 1 was generally greater than that in Section 3. The shear stress first increased and then decreased with increasing ice content when the ice content was <10 %. When the ice content was >10 %, the shear stress increased continuously, which was significant in Section 2. These findings illustrated that ice enhanced the increase in the shear stress. The shear stress depended on the variation of the flow depth and the density of the *DFI*. The results in section 3.2.2 indicated that the flow depth showed a slightly increasing trend at high ice content, while the density decreases with increasing ice content, which demonstrated that the flow depth mainly affected the shear stress. At Section 2, the shear stress was negative after erosion. The location covered by the bed soils was at Section 2. The basal stress measured by the represented by triaxial sensors represented the stresses in all bed soils at this position, and we set them to the 0 points. The bed soils were entrained, resulting in the mass of the bed soils being less than in the initial conditions, and therefore the stresses at this location exhibited negative values after erosion. This result revealed that the soil beds were eroded. For different ice contents, the shear stresses after erosion were − 0.018, −0.044, −0.076, −0.049 and − 0.054 kPa. The greater the negative value, the higher the mass of the bed soil being entrained.

Fig. 8 shows the variations in the normal stress in Sections 1–3. The normal stress first decreased but then increased for different ice contents along the channel. The normal stress in Section 1 was greater than that in Section 3. The normal stresses in Section 2 were 0.618, 0.457, 0.585, 0.453 and 0.577 kPa, which less than the normal stress at Section 1. There were two main reasons, one is that the bed soils are loosely packed, and when the *DFI* moved through the bed surface, a portion of the stresses cause the bed soils to be compacted. As a result, the normal stress at section 2 was reduced. On the other hand, at the upstream of Section 2, some of the *DFI* may silt up, resulting in the normal stress reduced at this location. Although accompanied by deposition and the bed soils being compacted, the *DFI* was predominantly eroded as it flowed over the surface of the soil beds. Therefore, the normal stress after erosion increased significantly compared with that before erosion. This can be evaluated from the normal stress in Section 2 when it

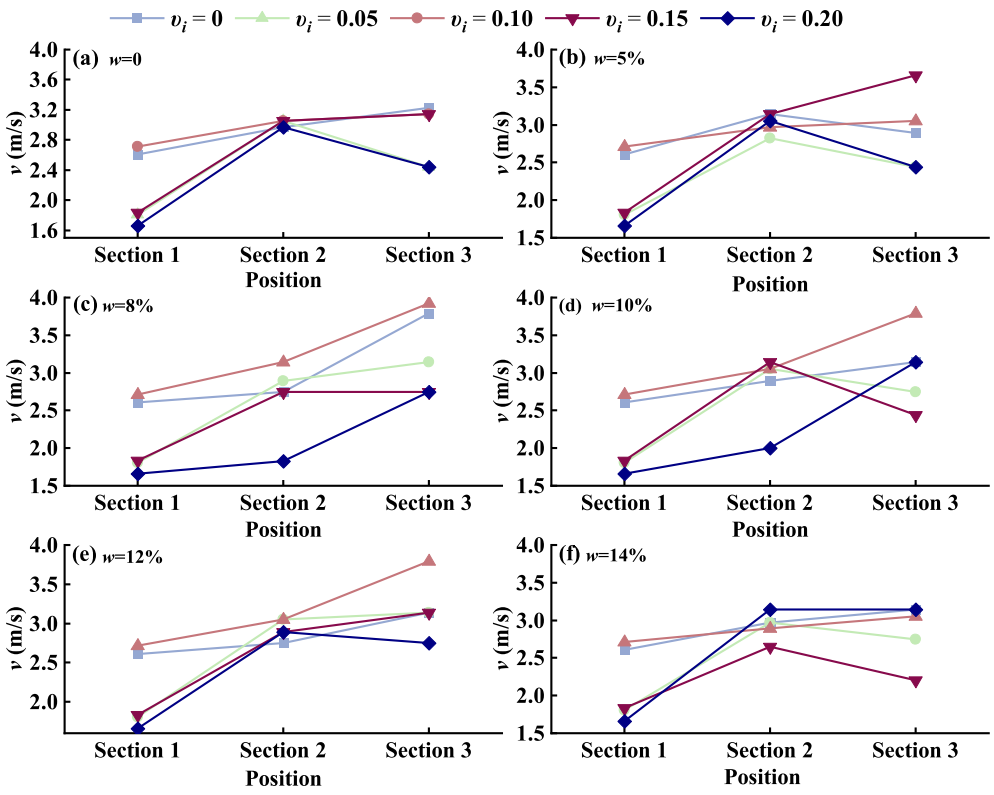

Fig. 6. Relationships between the velocity and ice contents and the water content of the soil beds in the different observation sections. (a)-(f) The water content of bed soil was 0, 5 %, 8 %, 10 %, 12 % and 14 %, respectively.

reached a steady state. The normal stress decreased by 0.217, 0.247, 0.259, 0.287 and 0.344 kPa compared with that before erosion. This result indicated that the erosion mass increased with increasing ice content. The normal stress reached a maximum when the ice content was 10 %. The effects of the ice content on the normal stress were minor for the other ice contents.

Fig. 7 and Fig. 8 all illustrated that the effects of ice contents on the basal stress. The shear and normal stresses showed the same evolutionary trends with ice content at section 1 and 3, but were different at section 2. These were governed by the characteristics of the bed soils. When the *DFI* interacted with the bed soil, the fluid transferred the force through the bed soil to the sensor at the bottom of the flume. During this process, deflections due to mutual shear will also occur between the interior of the bed soils, resulting in an increase in shear stress at Section 2 (Fig. 7). As mentioned above, the normal stress at Section 2 will decrease (Fig. 8).

3.2.4. *Pore pressure variation of DFI before and after erosion*

Pore pressure influences the mobility of debris flows by regulating their effective stresses (Song et al., 2023). Fig. 9 shows the variations in pore pressure before and after erosion along the channel. In Section 1, the soil beds were not eroded by the *DFI*, and the pore pressure was independent of the water content of the soil beds. Therefore, the pore pressure obtained in the experiments with soil beds with different water contents was averaged and used as the pore pressure of the *DFI* in Section 1 (Fig. 9a). With increasing ice content, the pore pressure steadily fluctuated, with values ranging from 0.44 to 0.57 kPa. In Section 3, the variations in the pore pressure were similar to those in Section 1. The pore pressure was the highest for the 10 % ice content, with values ranging from 0.32 to 0.87 kPa. This indicated that the pore pressure before and after erosion did not change significantly. This result revealed that the effects of erosion on the pore pressure were limited.

(a) Pore pressure in Section 1. The red dashed line represents the fitted curve of the relationship between pore pressure of the *DFI* and ice content. (b) Pore pressure in Section 3.

3.2.5. *Characteristics of pore pressure of bed soils during erosion*

Fig. 10 shows the variations in the pore pressure of the soil beds as the *DFI* flowed over the surface of the soil beds. The pore pressure for a water content of zero was significantly greater than that for the other water contents. The pore pressures of the soil bed for other water contents were closer to each other. This result indicated that the correlation between erosion and the water content of the soil beds was low. The pore pressure reached minimum values of 0.201, 0.108, 0.081, 0.074, 0.053 and 0.012 kPa when the water content was 15 %. The minimum pore pressure decreased continuously with increasing ice content. The maximum pore pressures were 0.599, 0.216, 0.166, 0.207, 0.180 and 0.150 kPa for each water content of the soil beds. For higher ice contents, the pore pressure was lower when the *DFI* eroded the soil beds.

3.3. *Relation between erosion and flow regime and shear stress*

3.3.1. *The erosion rate variation*

The erosion depth (H_e, unit: m) is an indicator that directly reflects the entrainment of the soil beds, which changes with the ice content. The erosion rate (E) is defined as the ratio of the average erosion depth to the erosion time. The erosion time is deduced by tracking the flow front through a top-view high speed camera, as the flow front moves through the entire erodible section. The erosion rate (E) was used to characterize the entrainment of the soil beds in this study (Fig. 11). The erosion rate (E) was the highest when the water content of the soil beds was zero. For ice contents <10 %, the differences in erosion rates for different water contents were small. When the ice content was >10 %, the erosion rate changed sharply with increasing ice content and generally decreased with increasing ice content. The erosion rate exhibited a parabolic relationship with the ice content. Therefore, the *DFI* with no ice or for

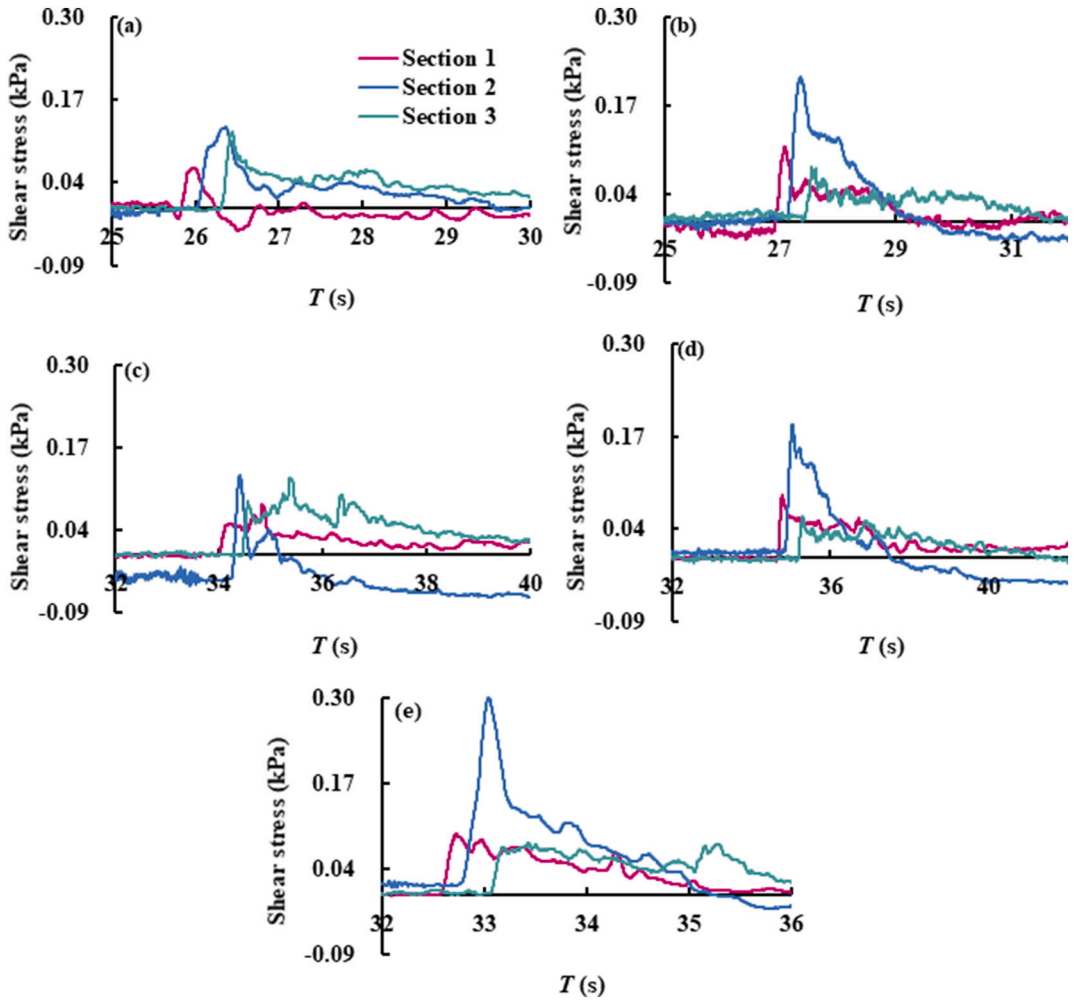

Fig. 7. Shear stress measured for different ice contents when the water content of the soil bed was 8 %. (a) ~ (e) The ice content of *DFI* was 0, 5 %, 10 %, 15 % and 20 %, respectively.

higher ice contents resulted in a lower erosion capacity. Fig. 11 showed that the relationship between the median erosion rate for each boxplot and ice content was used to represent the overall the relationship between the erosion rate of *DFI* and ice content. The median erosion rate at each ice content is in the range of 0.059–0.072. Although the difference in erosion rates is small, it clearly shows the relationship between the erosion rate and ice content. Similarly, the erosion rate exhibited a parabolic relationship with the volumetric moisture content of the bed soils. Song and Choi (2021) have also reported the same results. This demonstrated that the nearly saturated or dry bed soils will be more easily eroded.

The A_{me} values for different ice contents are listed in Table 2. A_{me} values were greater than unity, indicating that erosion in the upper half of the bed was greater than that in the lower half of the bed. The reason was that the upper half of the bed was in the transformed stage of erosion energy, and erosion was high (Song and Choi, 2021). When the *DFI* flowed through the lower half of the bed, its behaviour may be ascribed to the flow behaviour over the erodible bed, which means that it was influenced by the velocity (de Haas and Woerkom, 2016). The results revealed a nonlinear relationship between A_{me} and ice contents of the flow, and water contents of the soil beds.

3.3.2. *Correlation of the erosion rate variation and flow regime and shear stress*

Table 1 and Fig. 4 show that the density and physical parameters varied with the flow behaviour for different ice contents. This influenced the erosion of the *DFI*. Flow behaviour, including frontal velocity, flow depth and shear stress, had important effects on erosion (de Haas et al., 2022). The velocity and flow depth first increased but then decreased with increasing ice content. However, the velocity was greater for a 20 % ice content than for a 0 % ice content, whereas the flow depth exhibited the opposite trend. This result was different from the results of Wang et al. (2023). This difference may be attributed to the designated ice contents. Wang et al. (2023) held the rock volume constant and changed the ratio of the ice content to fluid. In this study, the volume of the *DFI* remained constant, and the ratio of the ice content to debris flow material was changed. The concentrations of solids in the debris flow materials were also held constant. In addition, the particle size distribution and concentration of solids in the *DFI* were significantly affected by ice. This resulted in an increase in the coarse particle content and a decrease in the fine particle content. The flow depth increased, and the velocity decreased accordingly (Roelofs et al., 2022). These factors controlled the flow depth and velocity. However, this result indicated that the mobility of the *DFI* had not reached a maximum for the higher ice content in this study.

The impact force and shear stress are the two main driving forces for erosion (de Haas et al., 2022; Roelofs et al., 2022). The shear stress is dependent on the density, flow depth, gravity and channel slope (de Haas and Woerkom, 2016). The impact force is influenced by the velocity, flow depth, and the velocity structure in the flow (Farin et al., 2019). When ice was present in the *DFI*, the shear stress was greater than that with no ice. This resulted from the compositional change in the *DFI*

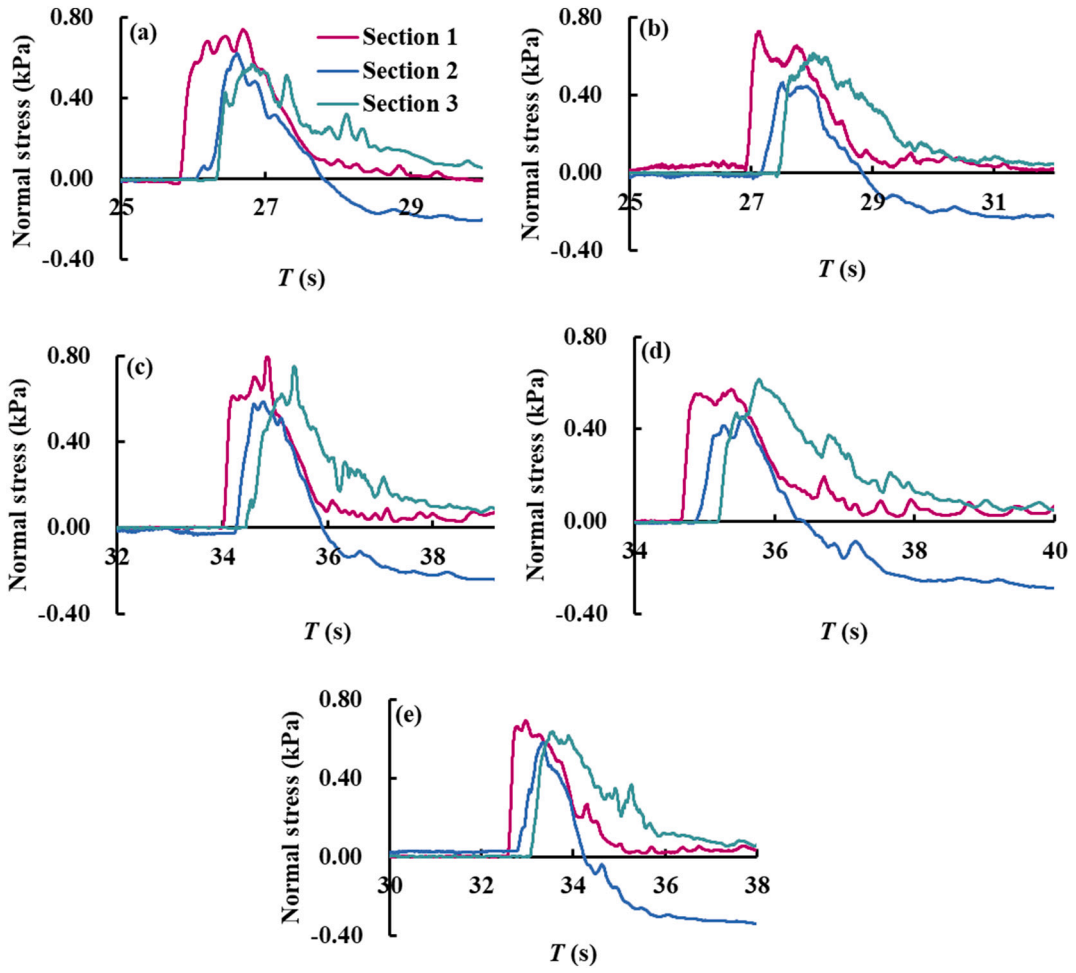

Fig. 8. Normal stress measured for different ice contents when the water content of the soil bed was 8 %. (a)-(e) The ice content of *DFI* was 0, 5 %, 10 %, 15 % and 20 %, respectively.

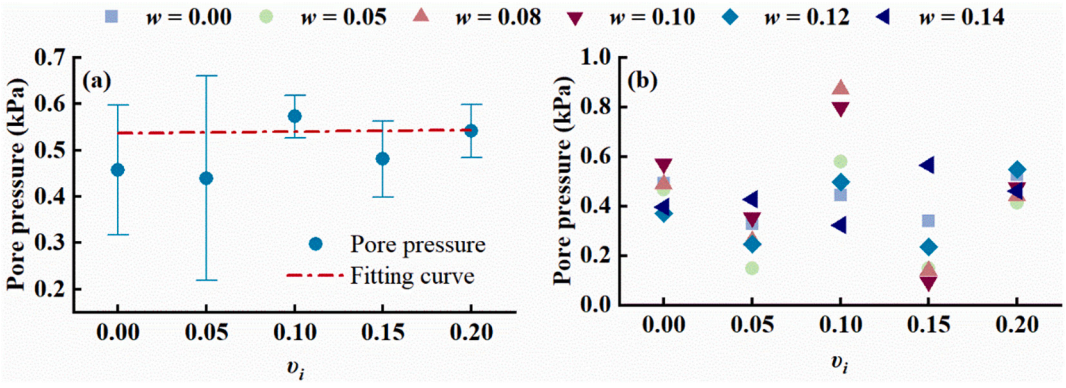

Fig. 9. Variations in the pore pressure with different ice contents before and after erosion.

when ice was present. This described the variation of shear stress before the *DFI* reached an erodible bed. Fig. 5 showed that the flow depth of higher ice content fluids was larger than the lower ice content. This resulted in the higher shear stress production as ice existed. This phenomenon was also due to the increase in the coarse particle content of the fluid as the ice content increases. The results were consistent with the research of Roelofs et al. (2022), who has reported that the shear stress of the fluid increases with increasing gravel content and solids volume concentration in the debris flow. The impact force was not measured in this study. The relationship between the N_S and ice contents revealed that the flow regime was dominated by collisional stress with increasing ice content. These results are consistent with the findings of Roelofs et al. (2022).

To investigate the internal dynamics of the *DFI* as they relate to erosion, we compared the dimensionless parameters with the ice contents. The flow regime transformed into grain collision-dominated flow with increasing ice content. The flow regime of the viscous stress-dominated flow gradually weakened. When the ice content was zero, the values of each dimensionless parameter were similar to those reported in previous studies (Roelofs et al., 2023; Zheng et al., 2021).

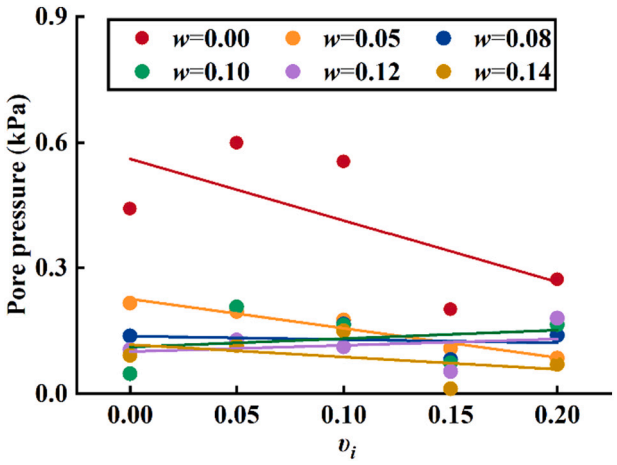

Fig. 10. Measured pore pressure of the soil bed during erosion.

When the ice content increased, on the one hand, the coarse particles increased, resulting in a flow regime dominated by interactions between particles. This result was basically consistent with the results of Roelofs et al. (2023). On the other hand, when the ice content increased, the water content of the fluid decreased, which also weakened the viscous stress.

The influence of ice on the dynamical characteristics of the *DFI* governs the erosion. This is attributed to the fact that the ice affects the exchange of mass and kinetic energy between the fluids and between the fluids and the basal materials in *DFIs*, which in turn affects erosion (Pudasaini, 2024). The relationships among the characteristics of movement, erosion, and ice contents were analysed (Fig. 12). A higher velocity corresponded to more intense erosion in the experiment. This was in agreement with the results that erosion enhances mobility of the debris flow as proposed by Pudasaini and Krautblatter (2021). The erosion was less as the higher ice contents. However, an increase in N_B, N_S, N_{fric}, N_M, N_R and τ induced a decrease in erosion. This increased the concentration of solids and coarse particles (Table 1). These results are similar to those of previous studies (Roelofs et al., 2023). However, several differences existed. The reason for these differences was that the influence of the concentration of solids and coarse particles on erosion had a secondary overlapping effect. This meant that the factors influencing the erosion of the *DFI* did not play an independent role.

Moreover, following the work of Wang et al. (2023), a higher ice content led to a change in the ice/water fraction in the *DFI*, which subsequently influenced erosion. This was mainly because the study of Wang et al. (2023) showed the ice/water content in the *DFI* influences their mobility. The higher the ice content in the fluid, the lower the water content, resulting in a less mobility of the fluid. This further will affect the erosion process.

3.4. Response of erosion to the flow behaviour of the DFI

The feedback effect of soil beds on erosion strongly influences flow behaviour (Zheng et al., 2021). Previous studies have investigated changes in debris flow behaviour only before and during erosion. However, comparisons of debris flow characteristics before and after erosion have been limited. We investigated the changes in the *DFI* properties before and after erosion, which can reveal the response of erosion to flow behaviour.

Figs. 4~7 show the characteristics of the velocity, flow depth, pore pressure and shear stress before and after erosion. To clarify the effects of erosion on the flow behaviour of the *DFI*, the relationship between the increase in the dynamic parameters and the erosion depth was illustrated (Fig. 13). The flow depth and velocity after erosion were greater than those before erosion (Fig. 13a and Fig. 13b). The shear stress and pore pressure were not significantly influenced by erosion (Fig. 13c and Fig. 13d). A positive relationship between the erosion rates and the flow depth, shear stress, and increase in the pore pressure can be revealed, and they all decreased with increasing ice content. However, a negative relationship between the erosion rate and velocity was observed. The high ice content induced a greater increase in velocity, whereas the flow depth, shear stress and pore pressure increased less. However, the initial velocity of the *DFI* for high ice contents was low. It can be inferred that the higher the ice content is, the more significantly it enhances the mobility of the *DFI*. The duration of *DFI* flow through the bed decreases with increasing ice content. The *DFI* can obtain more kinetic energy. Therefore, the increase in velocity with increasing ice content was greater than that with decreasing ice content. In addition, erosion can increase the mobility of *DFIs* (Pudasaini and Krautblatter, 2014; Wang et al., 2023) and subsequently increase the velocity. However, the flow depth, shear stress and pore pressure are influenced by the flow behaviour, soil bed properties and other factors, leading to insignificant effects of erosion. The above discussion indicates that the response of erosion to the behaviour of the *DFI* was characterized primarily by a

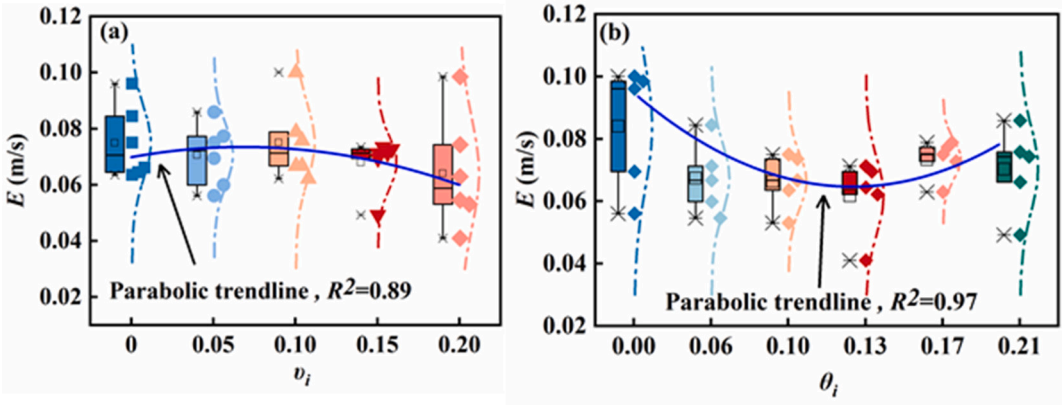

Fig. 11. (a) Erosion rate varying with the ice content for soil beds with different water contents. In each box plot, we put together a comparison of the erosion rates of the *DFI* of the same ice content as they erode bed soils of six water contents. The relationship between the median erosion rate for each boxplot and ice content was used to represent the overall the relationship between the erosion rate of *DFI* and ice content. The solid blue line represents the fitted curve of the relationship between the median erosion rate and ice content. (b) Erosion rate varying with the volumetric moisture content of the soil bed. In each boxplot, we put together a comparison of the erosion rates of the *DFI* with different ice contents as they erode the bed soils of the same water content. The solid blue line represents the fitted curve of the relationship between the median erosion rate and the volumetric moisture content. (For interpretation of the references to colour in this figure legend, the reader is referred to the web version of this article.)

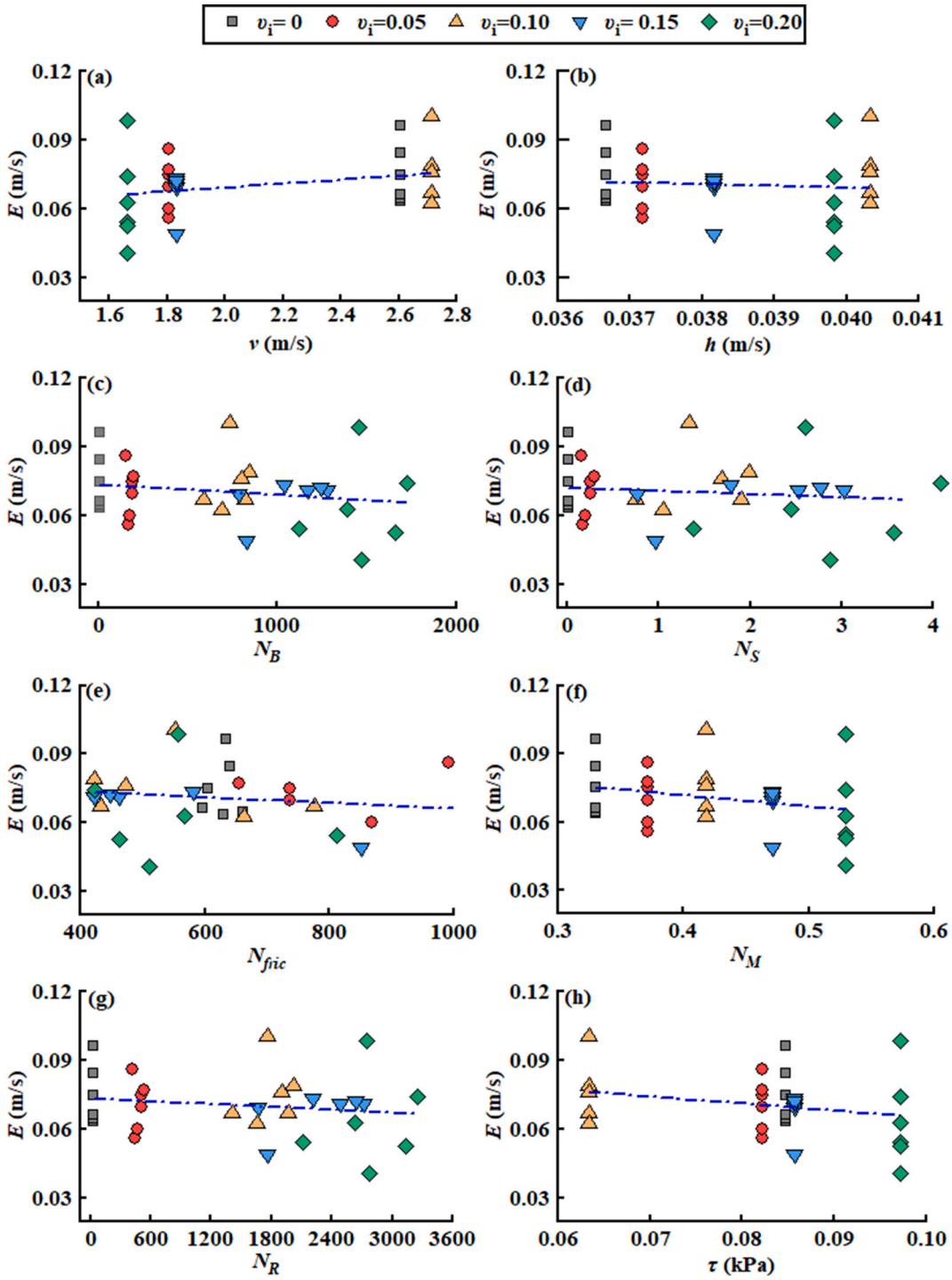

Fig. 12. Relationship between the erosion rate and behaviour of the *DFI*.

contribution to the increase in the flow velocity.

3.5. Erosion mechanism of the DFI

Soil bed properties are the other important factor controlling the erosion (Pudasaini, 2024).. Soil beds in nature are rarely saturated or fully dry, especially considering the fact that most debris flows occur during rainfall or glacier ice melting. And bed soil is in unsaturated condition. It is necessary to focus on the effect of the water content of the bed soils on the erosion (de Haas et al., 2022; Pudasaini and Fischer, 2020a; Pudasaini, 2024; Roelofs et al., 2023; Song and Choi, 2021). Six groups of soil beds with different water contents were used in the experiment. Fig. 11 shows that the dry bed was easily eroded. For the soil beds with other water contents, a nonlinear relationship between erosion and the water content occurred. This result was consistent with the results of Song and Choi (2021), who reported that parts of channels that are nearly saturated or dry are more easily eroded. This is because the saturated or dry bed soils were mechanically weaker in relation to the flowing materials itself. The relatively weak bed effectively reduces frictional stresses. This reduced stress, a positive quantity, is consistently and strictly balanced by the system, matching the additional (produced) momentum and eroded mass (Pudasaini, 2022; Pudasaini and Fischer,

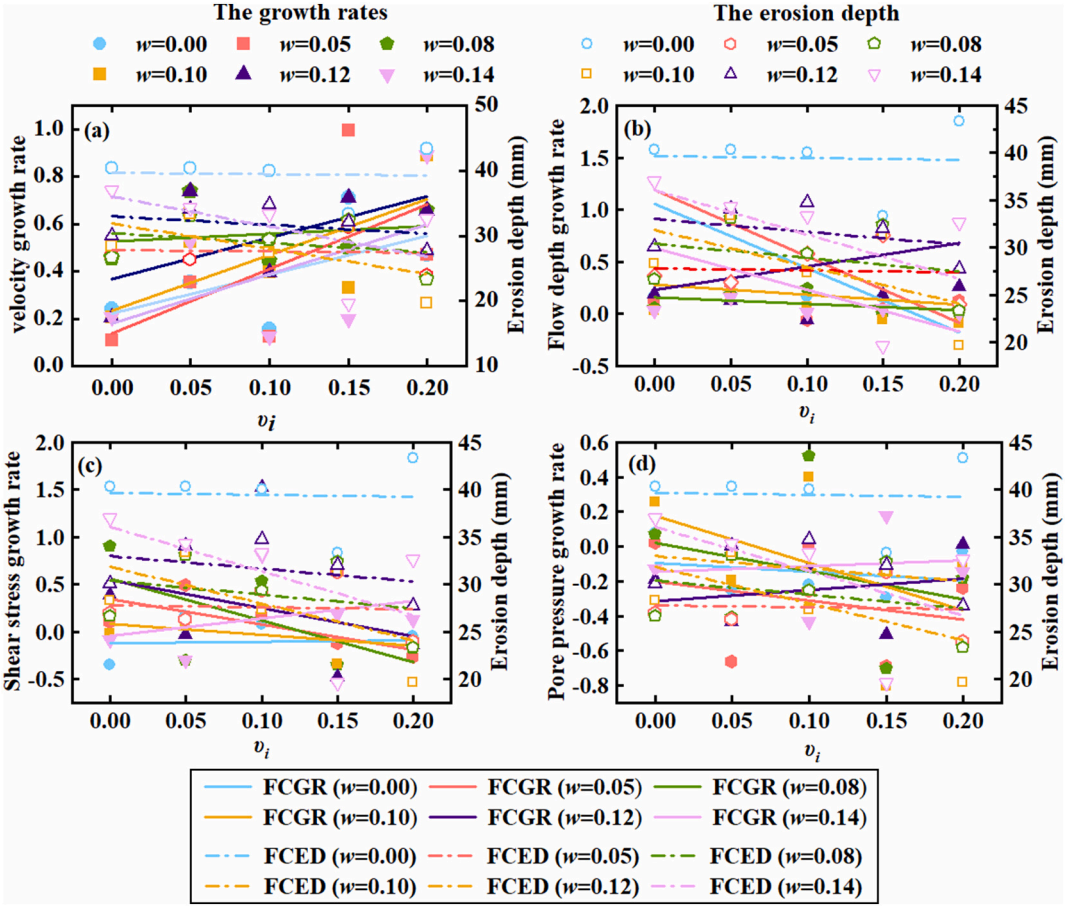

Fig. 13. Variations in growth rates of dynamic parameters and erosion depth with the ice content for soil beds with different water contents. The solid symbols and lines represent the growth rates and the fitting curve (FCGR) of dynamic parameters, and the dotted symbols and lines (FCED) represent the erosion depth.

2020a). This consequently results in erosion occurring. This conclusion was also revealed in this study and was especially significant for a 20 % ice content. Previous studies adopted saturated soil mechanics to describe the failure of the soil bed. The resistance of the soil beds (τ_b) can be calculated according to the Mohr–Coulomb criterion and is expressed as follows:

$$\tau_b = (\sigma - p)\tan\varphi + c \tag{11}$$

Where p is the pore pressure of the bed soil (kPa), σ is the normal stress (kPa),φ is the internal friction angle for the bed soil (°), c is the cohesion of the bed soil (kPa). The bed soils in this study are loose soils, the cohesion is considered to be zero. Eq. (11) indicates that the effective stress and strength of the saturated soil decrease with increasing pore pressure. However, soil beds in nature are rarely saturated. An unsaturated soil mechanics framework was proposed to characterize soil bed erosion by debris flows (Choi and Song, 2023; Song and Choi, 2021; Song et al., 2024). The strength of unsaturated soil can be expressed as follows:

$$\tau_b = (\sigma - p_a)\tan\varphi' + \kappa(p_a - p)\tan\varphi' \tag{12}$$

where p_a is the air pressure in pores (kPa), κ is a constant, can be represented by the saturated degree Sr. φ' is the internal friction angle of the soil (°). The matric suction provides additional strength for the unsaturated soil bed, and its strength is greater than that of nearly dry soil and fully saturated soil. When the values of the normal stress and pore pressure of the soil beds measured in the tests were substituted into Eq. (12), the shear strength of the soil bed (τ_b) was greater than the shear stress exerted by the *DFI* in some experiments. This finding illustrated that erosion of the soil bed may not be correlated with its water content. Song et al. (2024) reported that the erosion rate was independent of the water content of the bed because the water content affected only the uppermost soil particles, which immediately became saturated once the debris flow moved over them. The fluid infiltrated and saturated the surface of the soil bed, where erosion occurred. Therefore, the critical Shields number Θ_c can be used to describe the resistance of an initially unsaturated soil bed to erosion.

$${\tau_b}^u = \Theta_c(\rho_s - \rho)gD \tag{13}$$

Following the work of Prancevic et al. (2014), Θ_c can be set to 0.15. D can be denoted by D_{50}.

Erosion models of debris flows assume that the erosion rate is mostly determined by the availability of momentum transferred from the debris flow to the soil bed. The total shear stress ($\tau_c + \tau_e$) is the sum of the shear stress (τ_c) exerted by the debris flow and the component (τ_e) of weight of the eroded layer of the soil bed in the flow direction. The total shear stress can be expressed as follows:

$$E_c^u = \frac{\tau_c + \tau_e - {\tau_b}^u}{\rho v} = \frac{\tau + \rho_b g H_e \sin\theta - {\tau_b}^u}{\rho v} \tag{14}$$

where H_e is the erosion depth (m). In this study, the erosion rate was measured in the tests, and the other mechanical parameters were obtained via sensors. To evaluate the applicability of the measured data, a comparison between the measured erosion rate and that calculated via Eq. (14), the single-phase erosion model, and the two-phase erosion model was performed. The mechanical parameters of the single-phase erosion model and two-phase erosion model were obtained via theoretical methods of calculation.

(1) Single-phase erosion model.

Several single-phase mechanical models have been proposed (Iverson, 2012; Shen et al., 2020; Yang et al., 2018). The Voellmy model, which comprises shear and collisional stresses, was proven appropriate for describing the motion of granular debris flows.

$$\tau^{voel} = \rho g h \cos\theta \tan\varphi + \rho g (v/C_z)^2 \tag{15}$$

where C_z is the Chezy coefficient, defined by $C_z = h^{1/6}/n$, where n is the roughness coefficient. A typical value of 0.02 can be adopted on the basis of the field investigations of Cui et al. (2015). The soil bed is typically calculated according to the Mohr–Coulomb criterion and is expressed as follows:

$$\tau_b = (1-\lambda)\rho g h \cos\theta \tan\varphi + c \tag{16}$$

where λ is the pore pressure parameter, which can be calculated as follows: $\lambda = p/\rho g h \cos\theta$. c (kPa) is the cohesion force. The soil beds were in a loose state in this study. Therefore, the cohesion force equalled zero. The erosion rate can be expressed as follows:

$$E_c^{voel} = \frac{\tau^{voel} + \tau_e - \tau_b}{\rho v} \tag{17}$$

(2) Two-phase erosion model.

The solid and fluid phases and the strong interactions between the phases, including drag and viscous effects, were considered in the two-phase erosion model (Pudasaini and Fischer, 2020a; Pudasaini, 2022). The total erosion rate E_c^{tphase} comprises two aspects: the solid erosion rate E_s and the fluid erosion rate E_f. Here, the erosion rate for a solid can be expressed as follows:

$$E_s = \frac{g h \cos\theta \left[(1-\gamma^m)\rho_s^m \mu_s^m \alpha_s^m - (1-\gamma^b)\rho_s^b \mu_s^b \alpha_s^b\right]}{\left(\rho_s^m \lambda_{sl}^m \alpha_s^m - \rho_s^b \lambda_s^b \alpha_s^b\right) u_s} \tag{18}$$

where ($\gamma^m = \rho_f^m/\rho_s^m$, $\gamma^b = \rho_f^b/\rho_s^b$) are the fluid–solid density ratios, u_s is the mean velocity of the solids within the debris flow, and λ_{sl}^m and λ_s^b are the drift coefficients of erosion that connect the mean flow velocity (u_s) to the velocity in the lower layer of the debris flow ($u_{sl}^m = \lambda_{sl}^m u_s$) and the velocity of the eroded particles ($u_s^b = \lambda_s^b u_s$). The relationship between these two drift coefficients of erosion, as derived by Pudasaini and Fischer (2020a), is as follows:

$$\lambda_{sl}^m = \left(1 + \frac{\rho_s^b}{\rho_s^m}\frac{\alpha_s^b}{\alpha_s^m}\right)\lambda_s^b \tag{19}$$

By assuming that the upper debris mixture is a plug-like flow, the drift coefficient of erosion λ_{sl}^m can be approximately estimated as unity, and the mean velocity u_s equals the measured surface velocity v in the flume experiments.

The erosion rate for fluid can be expressed as follows:

$$E_f = \frac{\left[C_f^m \rho_f^m \left(\lambda_{fl}^m\right)^2 \alpha_f^m - C_f^b \rho_f^b \left(\lambda_l^b\right)^2 \alpha_f^b\right] u_f}{\left(\rho_f^m \lambda_{fl}^m \alpha_f^m - \rho_f^b \lambda_f^b \alpha_f^b\right)} \tag{20}$$

where C_f^m and C_f^b are the Chezy friction coefficients, and the value of C_g (0.022) is numerically adopted in this study on the basis of the constraints of previous studies (Li et al., 2024). u_f is the mean velocity of the fluids within the debris flow, and λ_{fl}^m and λ_f^b are the drift coefficients of erosion. Considering a simple situation as the fluid velocity within the bed sediments can be negligible, then Eq. (18) reduces to the simple expression for the erosion rate factor (Li et al., 2024):

$$E_f = C_f^m \lambda_{fl}^m u_f \tag{21}$$

For a plug-like debris flow, u_f equals the measured surface velocity v, and the drift coefficient of erosion λ_{fl}^m can also be approximately estimated as unity. The physical properties of the debris flow and the soil beds are listed in Table 1. μ_s^b is the effective Coulomb friction coefficient of the soil beds, which is related to the water content of the soil bed.

The calculated and measured erosion rates were analysed and are presented in Fig. 14. As can be inferred, the calculated erosion rates E_c^{tphase} and E_c^u were close to the measured erosion rates, whereas E_c^{voel} deviated. This is consistent with the results of Li et al. (2024), who has reported the two-phase erosion model was superior to single-phase model. This is because the debris flow and the erodible bed themselves typical are two-phase materials. The two-phase erosion model is based on the jump in the momentum flux and enhances an existing general two-phase erosion model (Pudasaini, 2012). It can better describe the erosion phenomena (Pudasaini and Fischer, 2020a).

The model proposed in this study that can describe unsaturated bed soils properties also has great applicability. Although the model is a single-phase flow model, we measured the variation of the basal stress and other mechanical parameters of the *DFI* during the erosion conducting the flume experiment, and considered the unsaturated characteristics of the bed soil. It can be realized from previous studies that the single-phase model still has applicability when the mechanical parameters measured in the experiment and the theoretical analysis parameters match those in the single-phase model (Lyu et al., 2024; Zhang et al., 2024; Qin et al., 2024). Although the two-phase model is preferable to

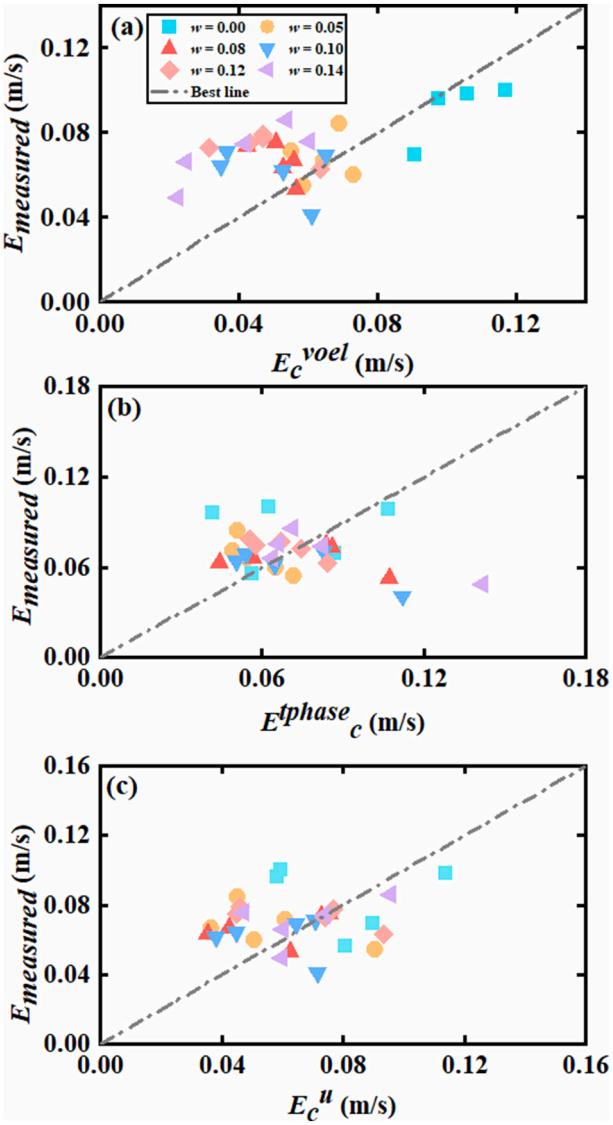

Fig. 14. Scatter plot between the calculated entrainment rates E_c^{voel}, E_c^{tphase}, and E_c^u and the measured average erosion rate E.

the proposed model, while the two are closer. Therefore, the proposed model is still applicable.

To further evaluate the applicability of the three models, three dimensionless performance indices were used: the mean average of the relative error (*MARE*), the Theil inequality coefficient (*TIC*), and the prediction accuracy factor (*PAF*) (Wang et al., 2018). They are given by the following:

$$MARE = \frac{1}{N}\sum_{i=1}^{N}\frac{\left|E_{cal,i} - E_{obs,i}\right|}{E_{obs,i}} \tag{22}$$

where N is the total number of data points used and $E_{cal,i}$ and $E_{obs,i}$ are the predicted erosion rate and observed erosion rate for case i, respectively.

$$TIC = \frac{\sqrt{\left(\sum_{i=1}^{N}\left(E_{cal,i} - E_{obs,i}\right)^2\right)/N}}{\sqrt{\left(\sum_{i=1}^{N}{E_{cal,i}}^2\right)/N} + \sqrt{\left(\sum_{i=1}^{N}{E_{obs,i}}^2\right)/N}} \tag{23}$$

$$PAF = 10^{\frac{\sum_{i=1}^{N}\left|\log\left(E_{cal,i}/E_{obs,i}\right)\right|}{N}} \tag{24}$$

The *MARE* and *TIC* indices range from 0 to 1, and lower *MARE* and *TIC* values denote better performance of the model. Additionally, a *PAF* value of 1.00 indicates that there is perfect agreement between all the calculated and measured values. According to Table 3 and Fig. 14, the unsaturated model (E_c^u) performed best, and it was applicable to be used to describe the erosion of the unsaturated soil beds when the *DFI* flowed over it.

The above results described the erosion mechanism of the *DFI*. When the *DFI* front flowed through the erodible section, the fluid infiltrated into the soil beds. Erosion occurs when the shear stress exerted by the *DFI* is greater than the strength of the unsaturated soil at the wetting front. The shift in the variable controlling erosion was rooted in the increase in shear stress, and net infiltration depth decreased as the flow velocity increased. However, the net infiltration depth increased over time to a magnitude where the shear stress was insufficient to mobilize the soil beds above the wetting front; thus, erosion stopped. This process was independent of the water content of the soil bed and was influenced by the relative magnitude of the infiltration rates of the fluid and the erosion rates (Song et al., 2024). The shear stress exerted by the *DFI* was related to the flow behaviour. The composition of the *DFI* influenced the flow depth and velocity, thus influencing the shear stress. This finding was discussed in Section 3.3.2. In other words, the erosion of *DFIs* is dependent on the flow behaviour for different ice contents and the rates of fluid infiltration in the soil beds.

4. Discussion

4.1. Effects of ice on the dynamic characteristics of the DFI

A *DFI* consists of solid (rock and ice) and fluid constituents. Compared with pure debris flows, ice may significantly influence the dynamics of *DFIs*. A *DFI* may consist of up to 20 % ice (Peng et al., 2022; Wang et al., 2023).

Three mechanisms that caused enhanced mobility of the rock–ice avalanche is proposed. (1) Reducing the friction and inducing fluidization within the propagating mass. (2) Frictional heating or compression of snow along the glacier elevates the basal fluid saturation. (3) Reduced friction at the debris-glacier interface (Pudasaini and Krautblatter, 2014). The ice content was lower in the *DFI*. Wang et al. (2023) reported that When ice content of *DFI* is less, the ice-water phase transition plays a minor role on the erosion. The reason for the phenomenon is the small initial ice content in the *DFI*. Ren et al. (2021), Wang et al. (2022) and Yang et al. (2019) have found that the average mass loss for each experiment was <0.1 %, indicating that no significant melting of the ice occurred and that the mixtures were nearly dry after each experiment. Therefore, the influence of the ice–water phase transition on erosion was minor. And in the experiment of this study, the flume experiment was used to study the erosion characteristics of the *DFI* on a shorter spatial and temporal dimension, where the fluid lasted for only a few seconds and melting the ice by frictional heat generation alone is very challenging. We also did not consider the effects of the phase transition, only the ice being treated as a low friction solid material.

When the ice existed, the physical parameter such as the *DFI* density ρ, the solid volume concentration υ_s, and the solid grain density ρ_s are all changed compared to it without ice. These are expressed as weighted averages of ice and the two-phase mixtures of soil and water. Following the work of Dong and Su (2024), Pudasaini and Krautblatter (2014) and Schneider et al. (2011), $\upsilon_s = \upsilon_r + \upsilon_i$ is the volume fraction of the solid, $\upsilon_s\rho_s = \upsilon_r\rho_r + \upsilon_i\rho_i$ is the effective solid mass, and $\rho = \rho_s\upsilon_s + \rho_f\upsilon_f$ is the density of *DFI*. The ice density is lower than the density of rock and water, leads to a decrease in both ρ and ρ_s with increasing ice content. And the ice, as solid material, is add to the *DFI*, increasing the solid volume concentration and particle size of the flow. This resulted in significant differences in the dynamics of the *DFI* from those in no ice, because the dynamics characteristics of the *DFI* depend on the composition of the flow (Roelofs et al., 2022). Specific analysis can be found in section 3.3.2.

The flow regime has the correlation with ice content. It is because the flow regime is closely related to the dynamic characteristics of the debris flow, which in turn also affect the variation of the flow regime (Iverson, 1997). The solid volume fraction of *DFIs* increases with increasing ice content. This results in the flow regime of *DFIs* being dominated by interparticle collisional stresses. However, the relationship between flow regime and ice content in the *DFI* is different from the relationship between rock-ice avalanche and ice content (Dong and Su, 2024). This is because the *DFI* contain much more water than rock-ice avalanche.

Ice influences the erosion by affecting dynamics characteristics and flow regimes of the *DFI*. Fig. 12 showed that there was a negative correlation between erosion rate and flow depth and flow regime, and a positive correlation with flow velocity. The results were consistent with the conclusion of Roelofs et al. (2022). The strict linear relationships between the erosion rate and these parameters were not showed, which was caused by the joint variation of the gravel fraction and the solid volume concentration in the *DFI*. Only gravel fraction or solids volume concentration change alone will not result in the same variation pattern of erosion characteristics. Roelofs et al. (2022) have reported that when gravel fraction increases, flow velocity decreases and the value of N_B and N_S increase, resulting in increased erosion. However, when υ_s increases, the flow velocity increases and erosion decreases. In this study, the gravel fraction and solids volume concentration of the *DFI* increased with increasing ice content. Therefore, the obviously correlation with the erosion rate and the flow regime is not showed.

Table 3
Comparison of the calculated entrainment rates E_c^{voel}, E_c^{tphase}, and E_c^u with the measured average erosion rate E.

Investigator	MARE	TIC	PAF
E_c^{voel}	0.34	0.08	1.42
E_c^{tphase}	0.30	0.07	1.33
E_c^u	0.33	0.06	1.35

4.2. Erosion mechanisms of the DFI

To evaluate the applicability of the erosion model proposed in this study, a comparison between the model of this study and the commonly used single-phase model and two-phase model was conducted.

The reason for choosing the two-phase model in this study is that both the debris flow and the bed soils are all two-phase materials. Although the *DFI* is a three-phase material of ice, water and soil

(Pudasaini, 2024), in this paper, the ice is regarded as a low-friction solid material that no melting during the erosion process. Therefore, the *DFI* can still be regarded as a two-phase material. Previous studies have demonstrated that the erosion phenomenon of the debris flow can be well describe by the two-phase model (Pudasaini, 2012, 2022; Pudasaini and Fischer, 2020a). Pudasaini (2024) have proposed a novel physically-based multi-phase thermo-mechanical model for rock-ice avalanche. The model is built on a multi-phase mass flow model and extends a two-phase rock-ice avalanche model. The reason for choosing the single-phase model is that strictly in terms of the erosion model proposed in this paper, it also belongs to the single-phase model. Sensors were used in this study to measure the mechanical parameters of the *DFI*, while it was not possible to measure the respective mechanical parameters of the solid and liquid phase separately. In comparison to the two-phase model, the single-phase model does not make physical meaningful due to the existence of singularities (Pudasaini and Fischer, 2020a). Notwithstanding the weaknesses of the single-phase model, it has been widely applied under specific experimental conditions (Lyu et al., 2024; Zhang et al., 2024; Qin et al., 2024). Although the experiments considered here are of two-phase nature, we considered those as single phase only for simplicity. Therefore, the single-phase model is reliable in this study. And a comparison with the proposed model with the commonly used single-phase model is necessary. The Voellmy model, which comprises shear and collisional stresses, was proved appropriate for describing the motion of granular debris flows (Rickenmann and Koch, 1997). Therefore, we selected the Voellmy model to make a comparison.

The results showed that the calculated E_c^u and E_c^{tphase} are approximate to the measured $E_{measured}$, whereas E_c^{voel} deviated (Fig. 14 and Table 3). Li et al. (2024) similarly compared the applicability of several erosion models and also found a deviation from the single-phase model. The results of Li et al. (2024) is consistent with the conclusion of (Pudasaini and Fischer, 2020a), who reported that singularities existed in the single-phase model. The analysis of this study concluded that it may have the following reasons: (1) τ^{voel} calculated by the Voellmy model is significantly higher than the measured τ^c (Fig. 7 and Attachment 1). (2) The Mohr-Coulomb criterion was used to calculate the shear resistance of the bed soil (Eq. (11)). This is the strength model of saturated soil, whereas the bed soils were unsaturated in this study. The strength of unsaturated soil is controlled by the matric suction (Fredlund and Rahardjo, 1993), which can be calculate by Eq. (12).

Song and Choi (2021) have used Eq. (12) to calculate the strength of unsaturated soil, and then the following erosion model was obtained:

$$E = K\frac{\upsilon_s \rho_s D_e^2 \dot{\gamma}^2}{\tau_b} \tag{25}$$

Where K is a coefficient related to the properties of the flow material.

Song and Choi (2021) have demonstrated that the collisional stress is the important force driving erosion, while the shear stress exerted on the erodible bed by the debris flow was not distinguished. The physical meaning of the coefficients K is not clearly defined. Therefore, the more rigorous erosion model is also needed.

In this study, the strength of the bed soil was calculated by either Eq. (11) or Eq. (12) greater than the measured the shear stress from the *DFI*. It results in the negative erosion rates. This indicated that the two strength models are all not appropriate. Song et al. (2024) have reported that the erosion mechanisms of water flow, and concluded that the erosion rate is independent of the bed water content, while it is related the infiltration of flow water. And mass failure is the main mechanisms used to describe soil bed erosion. Eq.13 used to calculate the strength of the unsaturated bed soils is appropriate. The results in this study showed the similar phenomena existed with the results of Song et al. (2024) during the erosion process (Fig. 15). Based on the above discussion, the erosion model for the *DFI* can be expressed by (Eq.14). The unsaturated bed soil, fluid infiltration, and the mechanisms of mass failure are considered in this model. The calculated E_c^u is closer to the measured erosion rate.

Two-phase model is a two-phase, process-based, non-singular mechanical model for erosion rates for both the solid and fluid phases (Pudasaini and Fischer, 2020a). It is based on the jump in the momentum flux and enhances an existing general two-phase mass flow model. At the interface, the solid stress satisfies the Coulomb law, and the fluid stress follows the Chezy-type friction. The erosion drifts were introduced in the model to represent the relationship between the mean flow velocity and the velocity of the solid- and liquid-phase materials in fluid and the bed soil. The value of the erosion drift coefficient is critical. In the solid erosion-rate model, the relationship between λ_{sl}^m and λ_s^b can be expressed by Eq.(19). We found that Eq.(19) used to explain the relationship between λ_{sl}^m and λ_s^b is not applicable. Therefore, after several trial calculations, the result showed that as $\lambda_{sl}^m \to \lambda_s^b$, and $\lambda_s^b \to 1$ (as $\lambda_{sl}^m = \lambda_s^b = 1$), the calculated E_c^{tphase} is most closer to the measured $E_{measured}$. This demonstrated that the erosion of the *DFI* is consistent with the characteristics of rapid erosion. Then the eroded particle moves with relatively higher velocity. At this situation, the relationship between the mean velocity of the debris flow and the velocity in the lower layer of the debris flow and the velocity of the eroded particles can be expressed by: $u_{sl}^m = u_s^b = u_s$. the fluid erosion-rate model can be given by Eq. (22). In general, λ_{fl}^m can be smaller than λ_{sl}^m and λ_s^b. Therefore, we assumed that $\lambda_{fl}^m = 0.5$. It was found that the erosion rate calculated by two-phase model was also closer to the measured erosion rate.

When the erosion occurred, the mass produced by erosion is added to the system moving together. Mass production leads to the corresponding momentum production, which is equivalent to the effectively reduced frictional stress (Pudasaini and Fischer, 2020a). The net momentum

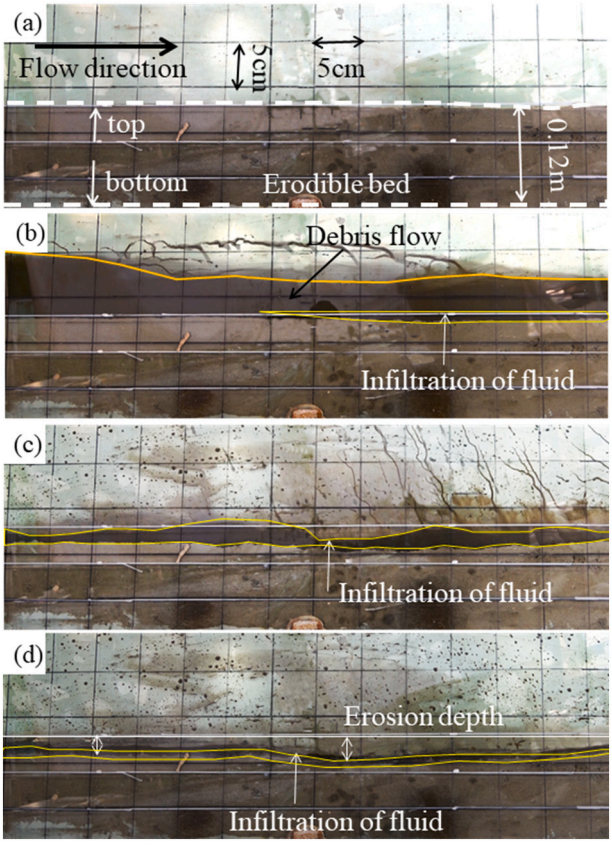

Fig. 15. Snapshots of debris flow erosion on the bed of the experiments. The debris flow is located on the solid orange line. The white dotted lines indicate the top and bottom of the erodible bed. The area outlined in yellow is the extent of fluid infiltration. (For interpretation of the references to colour in this figure legend, the reader is referred to the web version of this article.)

production and the gained potential energy due to added mass during the erosion eventually enhances the mobility of the debris flow (Pudasaini and Fischer, 2020a). The erosion of the *DFI* in this study is also characterized by this feature. Fig. 6 also showed that the velocity after erosion was higher than that before erosion and increased by 12.3 % ~ 99.6 %.

In sum, the two-phase model is the most desirable mechanical model for erosion rates (Pudasaini and Fischer, 2020a). To evaluate the applicability of the proposed model, we compare this with the two-phase model. From Table 3 and Fig. 13, although the two-phase model is preferable to the proposed model, while the two are closer. Therefore, the proposed model is still applicable.

4.3. Translation to Natural Flows

The erosion characteristics of the *DFI* were analysed in this study. To ensure that the results of the study can be applied to the field events, the soil samples were collected from a typical gully of a *DFI*. And the composition of the bed soils is same with the *DFI* material, which is also consistent with the actual situation in the field. The ice content of the *DFI* in this study is set to be <20 %, which is due to the fact that most of the rock-ice avalanches in real events have the initial ice content of 20 %–60 % (Zhou et al., 2024). A significant reduction in the ice content of the rock-ice avalanche occurs when it is transformed to a *DFI* downstream of the gully. The results of Schneider et al. (2011) showed that the rock-ice mixtures required an ice content of a least 60 % by volume to reach full liquefaction. A *DFI* is a mixture of rock-ice avalanche after it has become saturated. Therefore, it is hypothesized that the ice content in the *DFI* is much less than that in the initial rock-ice avalanche material, especially as the *DFI* moves to the mouth of the gully. This is consistent with the results of (Wang et al., 2023; Zhang et al., 2024), who reported the initial rock-ice avalanche in the zenongnong gully contained a total of 40 % water and ice content, whereas the *DFI* moved downstream with about 13 % ice content. The ice content designed for this study was also generally similar to field situation. The erosion enhances the mobility of the *DFI*, which is also consistent with the results of (Zhang et al., 2024).

As shown in Table 4, the dimensionless numbers representing flow behaviour for our experimental *DFI* vary within the ranges of values that developed in natural *DFI* and in natural general debris flows. This indicated that the flow behaviour of our experimental debris flows was largely similar to that of natural debris flows. However,

an uncertainty associated with the translation of our experimental results to natural *DFIs* events is that the erosion characteristics of the *DFI* at shorter spatial and temporal scales were analysed based on the flume experiment in this study. And when the initial ice contents of *DFI* is relatively high, there are also complex behaviors involved throughout the movement of the *DFI*, such as the melting of the ice and the heat generation phenomenon during the movement is an important question (Pudasaini, 2024). Therefore, the applicability of our results in field events has to be further investigated.

4.4. Limitations and future work

This study provided a preliminary analysis of the effect of the ice content on the dynamic and erosion properties of *DFI*. The results showed that erosion and fluid infiltration occur almost simultaneously during *DFI* movement. The erosion rate exhibited a parabola-like relationship with the ice content. Bed wetness has a positive feedback effect on erosion. However, there are some limitations of this study. (1) The results of this study were obtained based the flume experiments. Although the six dimensionless parameters were used to evaluate the flow dynamics of experimental and natural debris flows, the lack of real-time monitoring data on the *DFIs* and the possibility of some errors in the experiment itself lead to the fact that the applicability of the results of this study in describing real events in the field requires further investigation. (2) Although the reliability of the proposed model is closer to that of the two-phase model, it is still essentially a single-phase model, which does not have a strong physical meaning. (3) There are complex behaviors involved throughout the movement of the *DFI*, in particular the complex heat exchange processes across the avalanche body, basal heat conduction, the uniquely combined production and loss of heat due to the frictional shear heating and the ice melting, and the enhancement of the temperature associated with the entrainment of the basal material (Pudasaini and Krautblatter, 2014; Pudasaini, 2024).

There are a few simplifications in the design of the study. Complex thermodynamic phenomena during the *DFI* movement cannot be analysed based the present experiments. The new experimental instruments that can monitor temperature changes during the movement of the *DFI* and observe the movement of ice and the resulting melting phenomena are need to be designed in the future. The ice melting and heat exchange process were not considered during the erosion process. The results of Pudasaini (2024) has provided us with a better solution. Numerical simulation is also an effective method to analyse the motion characteristics of the *DFI*. In the future, In the future, based on the results of Pudasaini and Krautblatter (2014), Pudasaini and Fischer (2020a) and Pudasaini (2024), we will further analyse the phenomenon of ice melting during erosion process and the mechanism of its influence on

Table 4
Physical parameters and dimensionless numbers for the present laboratory experiments during erosion and for some natural events.

Parameter	Symbol (Unit)	Present tests	Natural debris flow			
			Chamoli (Shugar et al., 2021)	Kolka (Huggel et al., 2005, 2012)	Naltar Valley (Gardezi et al., 2022)	Natural debris flows (Iverson, 1997; Iverson and Denlinger, 2001; Zhou and Ng, 2010; Zheng et al., 2021)
Typical grain diameter	δ (m)	0.0081–0.0095	0.005	0.005	0.005	10^{-5}-10
Flow depth	h (m)	0.033–0.049	10	10	5	0.1–1
Flow shear rate	$\dot{\gamma}$ (1/s)	32.00–77.14	6	5	7	1–100
Solid density	ρ_s (kg/m^3)	1572–2760	2422	1666	2422	2500–3000
Fluid density	ρ_f (kg/m^3)	1332	1000	1400	1000	1000–1200
Solid volume fraction	C_v (−)	0.30–0.71	0.6	0.6	0.6	0.4–0.8
Fluid viscosity	η (Pa·s)	0.0018	0.00001	0.003	0.00001	0.001–0.1
Friction angle	φ (deg)	13.5–25.0	35	6	30	25–45
Froude number	Fr	2.22–4.84	6.06	5.05	5	0.5–7.6
Savage number	N_S	0.02–5.04	0.000919	0.00004	0.0025	10^{-7}-10^{0}
Bagnold number	N_B	10.71–1915.02	5,449,500.00	104.13	6,357,750.00	10^{0}–10^{8}

erosion. In addition, a large number of field investigations is needed to explore the real movement characteristics of the *DFI* and to prove the reliability of the experimental and numerical simulation results. This will facilitate a deeper understanding of the erosion characteristics of *DFIs*. And the results can be applied to the real *DFI* events.

5. Conclusions

A series of flume tests were conducted to analyse the dynamic characteristics of the *DFI* during erosion. On the basis of the results of this investigation, the following conclusions were drawn.

1. The dimensionless parameters (N_{Fr}, N_B, N_{fric}, and N_R) were used to characterize the flow regime of the *DFI*. All of them except N_{Fr} increased with increasing ice content. The presence of ice changed the characteristic grain size of the *DFI*. The flow regime was dominated by grain collisions.

2. The changes in the flow depth and velocity of the *DFI* after erosion were not significant compared with those of erosion but were greater than those before erosion. However, in the erodible section, the velocity increased compared with that before erosion. The higher the ice content was, the more significantly the velocity increased.

3. During erosion, the shear stress first increased but then decreased. The normal stress exhibited the opposite trend. When the ice content was <10 %, the shear stress first increased but then decreased with increasing ice content. In addition, the shear stress increased continuously as the ice content increased to >10 %. However, the growth rate of the shear stress before and after erosion was less influenced by the ice content.

4. The critical Shields number Θ_c can be used to describe the resistance of an initially unsaturated soil bed to erosion. A comparison between the calculated erosion rates of the three mechanical models and the measured erosion rates proved that the methods used to calculate the erosion rates of the *DFI* in this study and two-phase model were appropriate. However, the mechanical parameters of the *DFI* were measured. The model proposed in this study is more appropriate. The unsaturated bed soil, fluid infiltration, and the mechanisms of mass failure are considered in this model.

Supplementary data to this article can be found online at https://doi.org/10.1016/j.geomorph.2025.109835.

CRediT authorship contribution statement

Xiangning Li: Writing – original draft, Validation, Methodology, Formal analysis, Data curation. **Jiangang Chen:** Supervision, Funding acquisition. **Xiaoqing Chen:** Supervision, Funding acquisition. **Xi'an Wang:** Supervision. **Jinshui Wang:** Supervision. **Hechun Ruan:** Supervision. **Min Huang:** Supervision.

Declaration of competing interest

The authors have no conflicts of interest to declare.

Acknowledgements

This study was supported by the Second Tibetan Plateau Scientific Expedition and Research Program (Grant no. 2019QZKK0904), the Nyingchi National Sustainable Development Experimental Zone Project (2023-SYQ-007), the Science and Technology Research Program of Institute of Mountain Hazards and Environment, Chinese Academy of Sciences (Grant No. IMHE-ZDRW-02), and the Chinese Academy of Sciences Light of West China Program.

Data availability

The data that has been used is confidential.

References

Berger, C., McArdell, B.W., Schlunegger, F., 2011. Direct measurement of channel erosion by debris flows, Illgraben, Switzerland. J. Geophys. Res. :Earth Surf 116. https://doi.org/10.1029/2010jf001722 n/a-n/a.

Breien, H., De Blasio, F.V., Elverhøi, A., Høeg, K., 2008. Erosion and morphology of a debris flow caused by a glacial lake outburst flood, Western Norway. Landslides 5, 271–280. https://doi.org/10.1007/s10346-008-0118-3.

Choi, C.E., Ng, C.W.W., Au-Yeung, S.C.H., Goodwin, S.R., 2015. Froude characteristics of both dense granular and water flows in flume modelling. Landslides 12, 1197–1206. https://doi.org/10.1007/s10346-015-0628-8.

Choi, C.E., Song, P.J., 2023. New unsaturated erosion model for landslide: effects of flow particle size and debunking the importance of frictional stress. Eng. Geol. 315, 107024. https://doi.org/10.1016/j.enggeo.2023.107024.

Christen, M., Kowalski, J., Bartelt, P., 2010. RAMMS: Numerical simulation of dense snow avalanches in three-dimensional terrain. Cold Reg. Sci. Technol. 63, 1–14. https://doi.org/10.1016/j.coldregions.2010.04.005.

Cui, P., Zeng, C., Lei, Y., 2015. Experimental analysis on the impact force of viscous debris flow. Earth Surf. Process. Landf. 40, 1644–1655. https://doi.org/10.1002/esp.3744.

de Haas, T., Braat, L., Leuven, J.R.F.W., Lokhorst, I.R., Kleinhans, M.G., 2015. Effects of debris flow composition on runout, depositional mechanisms, and deposit morphology in laboratory experiments. J. Geophys. Res. Earth Surf. 120, 1949–1972. https://doi.org/10.1002/2015jf003525.

de Haas, T., McArdell, B.W., Nijland, W., Åberg, A.S., Hirschberg, J., Huguenin, P., 2022. Flow and Bed Conditions Jointly Control Debris-Flow Erosion and Bulking. Geophys. Res. Lett. 49. https://doi.org/10.1029/2021gl097611.

de Haas, T., Woerkom, T.V., 2016. Bed scour by debris flows: experimental investigation of effects of debris-flow composition. Earth Surf. Process. Landf. 41, 1951–1966. https://doi.org/10.1002/esp.3963.

De, J., Yao, T.D., Yao, P., Chen, Y.N., 2013. Characteristics of climate change in warm and cold periods revealed from ice cores and meteorological records during the past100years on the Tibetan Plateau. J. Glaciol. Geocryol. 35 (6), 1382–1390 (In Chinese). https://doi.org/10.7522/j.issn.1000-0240.2013.0153.

Dong, Z.B., Su, L.J., 2024. Flow regimes and basal normal stresses in rock–ice avalanches by experimental rotating drum tests. Cold Reg. Sci. Technol. 218. https://doi.org/10.1016/j.coldregions.2023.104081.

Dong, Z.B., Su, L.J., Hu, B.L., Miao, S.S., 2024. Friction behaviors and flow resistances of rock-ice avalanches. Cold Reg. Sci. Technol. 220. https://doi.org/10.1016/j.coldregions.2024.104130.

Evans, S.G., Bishop, N.F., Fidel Smoll, L., Valderrama Murillo, P., Delaney, K.B., Oliver-Smith, A., 2009. A re-examination of the mechanism and human impact of catastrophic mass flows originating on Nevado Huascarán, Cordillera Blanca, Peru in 1962 and 1970. Eng. Geol. 108, 96–118. https://doi.org/10.1016/j.enggeo.2009.06.020.

Farin, M., Tsai, V.C., Lamb, M.P., Allstadt, K.E., 2019. A physical model of the high-frequency seismic signal generated by debris flows. Earth Surf. Process. Landf. 44, 2529–2543. https://doi.org/10.1002/esp.4677.

Fredlund, D.G., Rahardjo, H., 1993. Soil mechanics for unsaturated soils. John Wiley & Sons.

Gao, B., Zhang, J.J., Wang, J.C., Chen, L., Yang, G.X., 2019. Formation mechanism and disaster characteristics of debris flow in the Tianmo gully in Tibet. Hydrogeol. Eng. Geol. 05, 144–153 (in Chinese). 10.16030/j.cnki.issn.1000-3665.2019.05.19.

Gardezi, H., Xing, A., Bilal, M., Zhuang, Y., Muhammad, S., Janjua, S., 2022. Preliminary investigation and dynamic analysis of a multiphase ice-rock avalanche on July 5, 2021, in the upper Naltar valley, Gilgit, Pakistan. Landslides 19, 451–463. https://doi.org/10.1007/s10346-021-01840-0.

Ge, Y.G., Cui, P., Su, F.H., Zhang, J.Q., Chen, X.Z., 2014. Case history of the disastrous debris flows of Tianmo Watershed in Bomi County, Tibet, China: some mitigation suggestions. J. Mt. Sci. 11, 1253–1265. https://doi.org/10.1007/s11629-014-2579-2.

Guo, R., Jiang, L.M., Xu, Z.D., Li, C., Huang, R.G., Zhou, Z.W., Li, T., Liu, Y., Wang, H.S., Fan, X.M., 2023. Seismic and hydrological triggers for a complex cascading geohazard of the Tianmo gully in the southeastern Tibetan Plateau. Eng. Geol. 324, 107269. https://doi.org/10.1016/j.enggeo.2023.107269.

Haeberli, W., Schaub, Y., Huggel, C., 2017. Increasing risks related to landslides from degrading permafrost into new lakes in de-glaciating mountain ranges. Geomorphology 293, 405–417. https://doi.org/10.1016/j.geomorph.2016.02.009.

Huggel, C., Clague, J.J., Korup, O., 2012. Is climate change responsible for changing landslide activity in high mountains? Earth Surf. Process. Landf. 37 (1), 77–91. https://doi.org/10.1002/esp.2223.

Huggel, C., Zgraggen-Oswald, S., Haeberli, W., Kääb, A., Polkvoj, A., Galushkin, I., Evans, S.G., 2005. The 2002 rock/ice avalanche at Kolka/Karmadon, Russian Caucasus: assessment of extraordinary avalanche formation and mobility, and application of QuickBird satellite imagery. Nat. Hazards Earth Syst. Sci. 5, 173–187. https://doi.org/10.5194/nhess-5-173-2005.

Iverson, R.M., 1997. The physics of debris flows. Rev. Geophys. 35, 245–296. https://doi.org/10.1029/97rg00426.

Iverson, R.M., 2012. Elementary theory of bed-sediment entrainment by debris flows and avalanches. J. Geophys. Res. Earth Surf. 117 (F3), 2011JF002189. https://doi.org/10.1029/2011jf002189.

Iverson, R.M., 2015. Scaling and design of landslide and debris-flow experiments. Geomorphology 244, 9–20. https://doi.org/10.1016/j.geomorph.2015.02.033.

Iverson, R.M., Denlinger, R.P., 2001. Flow of variably fluidized granular masses across three-dimensional terrain: 1. Coulomb mixture theory. J. Geophys. Res. Earth Surf. 106 (B1), 537–552. https://doi.org/10.1029/2000jb900329.

Iverson, R.M., Reid, M.E., Logan, M., LaHusen, R.G., Godt, J.W., Griswold, J.P., 2010. Positive feedback and momentum growth during debris-flow entrainment of wet bed sediment. Nat. Geosci. 4, 116–121. https://doi.org/10.1038/ngeo1040.

Li, P., Wang, J.D., Hu, K.H., Qiu, H.J., Xie, J.L., 2022b. Experimental investigation on debris flow resistance and entrainment characteristics: effects of the erodible bed with discontinuous grading. J. Mt. Sci. 19, 2397–2419. https://doi.org/10.1007/s11629-022-7365-y.

Li, P., Wang, J.D., Hu, K.H., Xie, J.L., 2024. Shedding effects of sediment composition and bed morphology on debris flow dynamics and entrainment mechanism: insights from laboratory experiments. Eng. Geol. 333, 107495. https://doi.org/10.1016/j.enggeo.2024.107495.

Li, Y., Cui, Y.F., Li, Z.H., Fu, X.D., 2022a. Evolution of glacier debris flow and its monitoring system along the Sichuan-Tibet Railway. Earth Sci. 06, 1969–1984 (in Chinese). https://doi.org/10.3799/dqkx.2021.194.

Lyu, B.H., Li, Y., Hu, P., 2024. Effects of bed sediment conditions on debris flow propagation from the two-phase flow modelling perspective. Adv. Water Resour. 183, 104592. https://doi.org/10.1016/j.advwatres.2023.104592.

McDougall, S., Hungr, O., 2005. Dynamic modelling of entrainment in rapid landslides. Can. Geotech. J. 42, 1437–1448. https://doi.org/10.1139/t05-064.

Monnier, S., Kinnard, C., 2015. Reconsidering the glacier to rock glacier transformation problem: New insights from the Central Andes of Chile. Geomorphology 238, 47–55. https://doi.org/10.1016/j.geomorph.2015.02.025.

Ng, C.W.W., Zheng, M., Liu, H., Poudyal, S., 2022. Effects of bed hydrophobicity on post-fire debris flow entrainment and momentum growth. J. Geophys. Res. Earth Surf. 127 (11), e2022JF006783. https://doi.org/10.1029/2022jf006783.

Peng, D.L., Zhang, L.M., Jiang, R.C., Zhang, S., Shen, P., Lu, W.J., He, X., 2022. Initiation mechanisms and dynamics of a debris flow originated from debris-ice mixture slope failure in southeast Tibet, China. Eng. Geol. 307, 106783. https://doi.org/10.1016/j.enggeo.2022.106783.

Prancevic, J.P., Lamb, M.P., Fuller, B.M., 2014. Incipient sediment motion across the river to debris-flow transition. Geology 42, 191–194. https://doi.org/10.1130/g34927.1.

Pudasaini, S.P., 2012. A general two-phase debris flow model. J. Geophys. Res. Earth Surf. 117 (F3), 2011JF002186. https://doi.org/10.1029/2011jf002186.

Pudasaini, S.P., 2022. Unified mechanical erosion model for multi-phase mass flows.

Pudasaini, S.P., 2024. A multi-phase thermo-mechanical model for rock-ice avalanche.

Pudasaini, S.P., Fischer, J.T., 2020a. A mechanical erosion model for two-phase mass flows. Int. J. Multiphase Flow 132. https://doi.org/10.1016/j.ijmultiphaseflow.2020.103416.

Pudasaini, S.P., Fischer, J.T., 2020b. A mechanical model for phase separation in debris flow. International Int. J. Multiphase Flow. 129, 103292. https://doi.org/10.1016/j.ijmultiphaseflow.2020.103292.

Pudasaini, S.P., Krautblatter, M., 2014. A two-phase mechanical model for rock-ice avalanches. Case Rep. Med. 119, 2272–2290. https://doi.org/10.1002/2014jf003183.

Pudasaini, S.P., Mergili, M., 2019. A multi-phase mass flow model. J. Geophys. Res. Earth Surf. 124, 2920–2942. https://doi.org/10.1029/2019JF005204.

Qin, S.W., Lv, J.F., Qiao, S.S., Chen, J.J., Yao, J.Y., Wan, F., Peng, S.Y., Rehman, G., Liu, X.W., 2024. Effects of bed pumice content on lahar erosion: an example from Changbaishan volcano, China. Eng. Geol. 336, 107560. https://doi.org/10.1016/j.enggeo.2024.107560.

Ren, Y., Yang, Q., Cheng, Q., Cai, F., Su, Z., 2021. Solid-liquid interaction caused by minor wetting in gravel-ice mixtures: a key factor for the mobility of rock-ice avalanches. Eng. Geol. 286. https://doi.org/10.1016/j.enggeo.2021.106072.

Rickenmann, D., Koch, T., 1997. In: Debris-Flow Hazards Mitigation: Mechanics, Prediction, and Assessment. In: Comparison of debris flow modelling approaches. ASCE, pp. 576–585 pp.

Roelofs, L., Colucci, P., de Haas, T., 2022. How debris-flow composition affects bed erosion quantity and mechanisms: An experimental assessment. Earth Surf. Process. Landf. 47, 2151–2169. https://doi.org/10.1002/esp.5369.

Roelofs, L., Nota, E.W., Flipsen, T.C.W., Colucci, P., de Haas, T., 2023. How Bed Composition Affects Erosion by Debris Flows—An Experimental Assessment. Geophys. Res. Lett. 50. https://doi.org/10.1029/2023gl103294.

Schneider, D., Kaitna, R., Dietrich, W.E., Hsu, L., Huggel, C., McArdell, B.W., 2011. Frictional behavior of granular gravel–ice mixtures in vertically rotating drum experiments and implications for rock–ice avalanches. Cold Reg. Sci. Technol. 69, 70–90. https://doi.org/10.1016/j.coldregions.2011.07.001.

Shen, P., Zhang, L., Wong, H.F., Peng, D., Zhou, S., Zhang, S., Chen, C., 2020. Debris flow enlargement from entrainment: a case study for comparison of three entrainment models. Eng. Geol. 270. https://doi.org/10.1016/j.enggeo.2020.105581.

Shen, Y.J., Chen, S.W., Zhang, L., Mang, P.H., Tian, S.S., Ma, W., 2022. High-altitude initiation, dynamic collapse and phase transformation of mountain snow-ice melt geological disaster chain. J. Glaciol. Geocryol. 44 (2), 643–656 (In Chinese). https://doi.org/10.7522/j.issn.1000-0240.2022.0066.

Shugar, D.H., Jacquemart, M., Shean, D., Bhushan, S., Upadhyay, K., Sattar, A., Schwanghart, W., McBride, S., de Vries, M.V.W., Mergili, M., Emmer, A., Deschamps-Berger, C., McDonnell, M., Bhambri, R., Allen, S., Berthier, E., Carrivick, J.L., Clague, J.J., Dokukin, M., Dunning, S.A., Frey, H., Gascoin, S., Haritashya, U.K., Huggel, C., Kaab, A., Kargel, J.S., Kavanaugh, J.L., Lacroix, P., Petley, D., Rupper, S., Azam, M.F., Cook, S.J., Dimri, A.P., Eriksson, M., Farinotti, D., Fiddes, J., Gnyawali, K.R., Harrison, S., Jha, M., Koppes, M., Kumar, A., Leinss, S., Majeed, U., Mal, S., Muhuri, A., Noetzli, J., Paul, F., Rashid, I., Sain, K., Steiner, J., Ugalde, F., Watson, C.S., Westoby, M.J., 2021. A massive rock and ice avalanche caused the 2021 disaster at Chamoli, Indian Himalaya. Science 373, 300–306. https://doi.org/10.1126/science.abh4455.

Song, D.R., Chen, X.Q., Sadeghi, H., Zhong, W., Hu, H.W., Liu, W., 2023. Impact behavior of dense debris flows regulated by pore-pressure feedback. J. Geophys. Res. Earth Surf. 128 (12), e2023JF007074. https://doi.org/10.1029/2023jf007074.

Song, D.R., Chen, X.Q., Zhou, G.G.D., Lu, X.Q., Cheng, G.W., Chen, Q., 2021a. Impact dynamics of debris flow against rigid obstacle in laboratory experiments. Eng. Geol. 291, 106211. https://doi.org/10.1016/j.enggeo.2021.106211.

Song, D.R., Zhou, G.G.D., Chen, Q., 2021b. Flow resistance in the transition from dense to dilute granular-fluid flows. Granul. Matter 23 (3), 73. https://doi.org/10.1007/s10035-021-01134-1.

Song, P.J., Choi, C.E., 2021. Revealing the importance of capillary and collisional stresses on soil bed erosion induced by debris flows. J. Geophys. Res. 126 (5), e2020JF005930. https://doi.org/10.1029/2020jf005930.

Song, P.J., Yang, J., Choi, C.E., Zhang, J.Q., 2024. Experimental investigation on scouring v.s. mass failure of unsaturated soil bed: implications for debris flow initiation and erosion. J. Geophys. Res. 129 (4), e2023JF007275. https://doi.org/10.1029/2023jf007275.

Sun, H., Zhao, W.Y., You, Y., Li, D.L., Liu, J.F., Wang, D.W., 2022. A study on debris flow dynamic behavior in a drainage channel with step-pool configuration. Landslides 19, 3031–3042. https://doi.org/10.1007/s10346-022-01942-3.

Takahashi, T., 2007. Debris flow: mechanics, prediction and countermeasures, 1st ed. Taylor & Francis. https://doi.org/10.1201/9780203946282.

Van Wyk de Vries, M., Bhushan, S., Jacquemart, M., Deschamps-Berger, C., Berthier, E., Gascoin, S., Shean, D.E., Shugar, D.H., Kääb, A., 2022. Pre-collapse motion of the February 2021 Chamoli rock-ice avalanche, Indian Himalaya. Nat. Hazards Earth Syst. Sci. Discuss. 22 (10), 1–29. https://doi.org/10.5194/nhess-22-3309-2022.

Wang, C.Y., Cui, Y.F., Song, D.R., Nie, J.Y., Hu, B.T., 2022. Effect of ice content on the interaction between rock–ice avalanche and rigid barrier: physical and numerical modelling. Comput. Geotech. 150, 104924. https://doi.org/10.1016/j.compgeo.2022.104924.

Wang, T., Chen, J.G., Chen, X.Q., You, Y., Cheng, N.S., 2018. Application of incomplete similarity theory to the estimation of the mean velocity of debris flows. Landslides 15, 2083–2091. https://doi.org/10.1007/s10346-018-1045-6.

Wang, T.F., Huang, T.S., Shen, P., Peng, D.L., Zhang, L.M., 2023. The mechanisms of high mobility of a glacial debris flow using the Pudasaini-Mergili multi-phase modeling. Eng. Geol. 322, 107186. https://doi.org/10.1016/j.enggeo.2023.107186.

Wang, W.P., Yang, J.S., Wang, Y.B., 2019. Dynamic processes of 2018 Sedongpu landslide in Namcha Barwa–Gyala Peri massif revealed by broadband seismic records. Landslides 17, 409–418. https://doi.org/10.1007/s10346-019-01315-3.

Yang, H.Q., Xing, S.G., Wang, Q., Li, Z., 2018. Model test on the entrainment phenomenon and energy conversion mechanism of flow-like landslides. Eng. Geol. 239, 119–125. https://doi.org/10.1016/j.enggeo.2018.03.023.

Yang, Q.Q., Su, Z.M., Cheng, Q.G., Ren, Y.H., Cai, F., 2019. High mobility of rock-ice avalanches: insights from small flume tests of gravel-ice mixtures. Eng. Geol. 260, 105260. https://doi.org/10.1016/j.enggeo.2019.105260.

Zhang, X.P., Hu, K.H., Liu, S., Nie, Y., Han, Y.Z., 2022. Comprehensive interpretation of the Sedongpu glacier-related mass flows in the eastern Himalayan syntaxis. J. Mt. Sci. 19, 2469–2486. https://doi.org/10.1007/s11629-022-7376-8.

Zhang, Y., Lyu, L., Ren, W., Wang, Z., 2024. Preliminary investigation on the kinetic characteristics of the glacial debris flows in Tianmo Valley, Tibet Plateau, China. J. Geophys. Res. Earth Surf. 129 (2), e2023JF007447. https://doi.org/10.1029/2023jf007447.

Zhao, C.X., Yang, W., Westoby, M., An, B.S., Wu, G.J., Wang, W.C., Wang, Z.Y., Wang, Y.J., Dunning, S., 2022. Brief communication: an approximately 50 Mm^3 ice-rock avalanche on 22 march 2021 in the sedongpu valley, southeastern Tibetan Plateau. Cryosphere 16, 1333–1340. https://doi.org/10.5194/tc-16-1333-2022.

Zheng, H.C., Hu, X.L., Shi, Z.M., Shen, D.Y., De Haas, T., 2024. Deciphering controls of pore-pressure evolution on sediment bed erosion by debris flows. Geophys. Res. Lett. 51. https://doi.org/10.1029/2024GL108583 e2024GL108583.

Zheng, H.C., Shi, Z.M., Yu, S.B., Fan, X.M., Hanley, K.J., Feng, S.J., 2021. Erosion mechanisms of debris flow on the sediment bed. Water Resour. Res. 57 (12), e2021WR030707. https://doi.org/10.1029/2021wr030707.

Zhou, G.G., Ng, C.W., 2010. Dimensional analysis of natural debris flows. Can. Geotech. J. 47 (7), 719–729. https://doi.org/10.1139/t09-134.

Zhou, G.G.D., Chen, L.L., Mu, Q.Y., Cui, K.F.E., Song, D.R., 2019. Effects of water content on the shear behavior and critical state of glacial till in Tianmo gully of Tibet, China. J. Mt. Sci. 16, 1743–1759. https://doi.org/10.1007/s11629-019-5440-9.

Zhou, G.G.D., Cui, K.F.E., Jing, L., Mangeney, A., Cui, Y., Huang, Y., Chen, X.Q., 2024. Segregation-induced flow transitions in rock-ice mixtures: implications for rock-ice avalanche dynamics. J. Geophys. Res:Earth Surf 129, e2024JF007831. https://doi.org/10.1029/2024JF007831.